

Effects of the Representation of Rimed Ice in Bulk Microphysics Schemes on Polarimetric Signatures

MARCUS JOHNSON AND YOUNGSUN JUNG

*Center for Analysis and Prediction of Storms, and School of Meteorology,
University of Oklahoma, Norman, Oklahoma*

JASON A. MILBRANDT

*Atmospheric Numerical Weather Prediction Research, Environment and Climate Change Canada,
Dorval, Quebec, Canada*

HUGH MORRISON

National Center for Atmospheric Research, Boulder, Colorado

MING XUE

*Center for Analysis and Prediction of Storms, and School of Meteorology,
University of Oklahoma, Norman, Oklahoma*

(Manuscript received 16 November 2018, in final form 24 July 2019)

ABSTRACT

Many flavors of multcategory, multimoment bulk microphysics schemes (BMPs) have various treatments of rimed ice. In this study, we compare three two-moment schemes available in the WRF Model—Milbrandt–Yau (MY2), National Severe Storms Laboratory (NSSL), and the two-category configuration of the Predicted Particle Properties (P3) scheme—focusing on differences in rimed-ice representation and their impacts on surface rain and ice. Idealized supercell simulations are performed. A polarimetric radar data simulator is used to evaluate their ability to reproduce the Z_{DR} arc and hail signature in the forward-flank downdraft, well-known supercell polarimetric signatures that are potentially sensitive to rimed-ice parameterization. Both the MY2 and NSSL schemes simulate enhanced surface Z_{DR} bands, but neither scheme simulates a Z_{DR} arc commonly identified in observation-based studies. Surface Z_{DR} in the default P3 scheme is homogeneous in the supercell's forward flank, and is due to the scheme's restrictive minimum rain particle size distribution (PSD) slope bound preventing the presence of larger drops creating a Z_{DR} arc. The NSSL scheme simulates the location of the hail signature in the forward-flank downdraft more consistent with observations than the other two schemes. Large hail in MY2 sediments well downstream of the updraft (atypically compared to observations) near the surface. The sedimentation of large ice in the default P3 scheme is limited by a restrictive maximum ice number-weighted mean diameter limit within the scheme, precluding the scheme's ability to reduce Z_{DR} (and ρ_{HV} compared to the MY2 and NSSL schemes) near the surface.

1. Introduction

Cloud microphysics is the collection of all hydrometeor processes spanning cloud particle formation to precipitation. These processes are very complex and highly nonlinear. Liquid phase processes are less complex and drops are well represented as constant density spheres, with the caveat that larger rain drops do slightly deviate

from this approximation with decreasing axis ratio (e.g., Pruppacher and Pitter 1971; Chandrasekar et al. 1988; Brandes et al. 2002). On the other hand, ice processes lack adequate observations and theoretical understanding that can explain their highly variable evolution in shape and density depending on temperature and ice supersaturation. This deficiency in complex ice phase, habit, and evolution information inevitably leads to large ice microphysical parameterization uncertainty in numerical weather prediction (NWP) models. Because ice processes

Corresponding author: Youngsun Jung, youngsun.jung@ou.edu

DOI: 10.1175/MWR-D-18-0398.1

© 2019 American Meteorological Society. For information regarding reuse of this content and general copyright information, consult the [AMS Copyright Policy](https://www.ametsoc.org/PUBSReuseLicenses) (www.ametsoc.org/PUBSReuseLicenses).

play a crucial role in simulations due to their impact on the radiation budget, thermodynamic fields, and storm dynamics, there have been many efforts to improve microphysical parameterization schemes in atmospheric models (e.g., Johnson et al. 1993; Liu et al. 2007; Milbrandt and Morrison 2013).

Although spectral bin microphysics schemes (SBMs) allow greater particle size distribution (PSD) characteristic flexibility (e.g., Takahashi 1976; Khain et al. 2004), current NWP models continue to employ bulk microphysics schemes (BMPs) because of their significant computational cost advantage and current lack of clear SBM advantage in convective simulation skill (Fan et al. 2017). Rather than predicting the binned PSD as in SBMs, BMPs assume analytic PSDs, generally gamma distributions, and predict moments of the distribution. Predicted moments update model information because they are typically linked to physical quantities (e.g., number concentration N_x is the zeroth moment of a PSD). BMPs are typically categorized by their number of predicted moments [i.e., one-moment schemes generally predict mass mixing ratio q_x , two-moment schemes add complexity by further predicting number mixing ratio (N_x), and so on]. Because two-moment schemes add particle distribution information, they can provide an improvement over one-moment schemes in convective-scale simulations in terms of cold pool structure, simulated polarimetric signatures, and hydrometeor size sorting (e.g., Milbrandt and Yau 2005a; Dawson et al. 2010; Jung et al. 2010, 2012; Putnam et al. 2017a), although the two-moment improvement is less clear for simulated cloud structure and surface precipitation (e.g., Wang et al. 2009; Varble et al. 2011; Van Weverberg et al. 2014). Three-moment schemes that additionally predict reflectivity Z have also been developed (Milbrandt and Yau 2005a,b; Dawson et al. 2014; Loftus et al. 2014), and simulate hydrometeor size sorting more consistent with observations than two-moment schemes with a fixed shape parameter (e.g., Milbrandt and Yau 2005a; Dawson et al. 2010; Kumjian and Ryzhkov 2012).

Traditional BMPs represent the wide variety of ice habits, with different shapes and densities, using two or more predefined ice hydrometeor types (i.e., pristine ice, snow, graupel, and/or hail). Specifically, the number of rimed-ice categories and their corresponding density and fall speed assumptions can differ considerably. Some BMPs contain a single rimed-ice category, employing either intermediate-density graupel or high-density hail (e.g., Wisner et al. 1972; Rutledge and Hobbs 1984; Ziegler 1985; Murakami 1990; Tao and Simpson 1993; Thompson et al. 2008; Morrison et al. 2009), while others contain both (e.g., Ferrier 1994; Walko et al. 1995; Milbrandt and Yau 2005b; Mansell et al. 2010).

In regard to rimed-ice parameterization, Morrison and Milbrandt (2011) found weaker cold pools, less surface precipitation, and enhanced anvils using two-moment graupel-like rimed ice rather than two-moment hail-like rimed ice in idealized supercell simulations. Newer BMPs have incorporated additional complexity by predicting rimed-ice particle volume in order to predict particle density (Mansell et al. 2010; Milbrandt and Morrison 2013), which might simulate supercells more accurately (Johnson et al. 2016). Recently, Morrison and Milbrandt (2015) proposed a new approach to represent ice-phase hydrometeors in microphysics schemes as “free” ice phase categories, rather than partitioning ice into several predefined categories, which requires assumptions about physical properties, the parameterization of ad hoc artificial conversion between categories, and other limitations.

Several previous studies have shown that simulated polarimetric variables can be used in evaluating microphysics scheme accuracy (e.g., Jung et al. 2010; Putnam et al. 2014; Johnson et al. 2016; Putnam et al. 2017a; Putnam et al. 2017b; Johnson et al. 2018), and are especially useful in a supercell framework due to their sensitivity to rimed-ice treatment. Dawson et al. (2014) showed that the Z_{DR} arc, a low-level maximum of differential reflectivity on the supercell’s edge caused by the size sorting of rain and rimed ice (Ryzhkov et al. 2005; Kumjian and Ryzhkov 2008, 2009), might be more sensitive to the parameterization of rimed ice rather than rain. Further, Johnson et al. (2016) found that the hail signature in the forward-flank downdraft (FFD), a region of low differential reflectivity near the surface due to dry, tumbling hail (Kumjian and Ryzhkov 2008), was best simulated when the medium-density rimed-ice category (i.e., graupel) acts as a feeder category to the high-density rimed-ice category (i.e., hail).

This study attempts to evaluate two different approaches to representing frozen hydrometeors (i.e., predefined and free ice-phase categories) in idealized supercell simulations, specifically the performance of the P3 scheme. This study focuses on a supercell storm because of its well-documented observed polarimetric signatures (we refer the reader to Ryzhkov et al. 2005 and Kumjian and Ryzhkov 2008 for observational examples of the supercell polarimetric signatures examined in this paper). As rimed ice has a greater influence on the polarimetric signatures near the surface than pristine ice and snow, discussion will mainly focus on rimed ice. Two two-moment BMPs with two traditional rimed-ice categories (graupel and hail), the Milbrandt–Yau (MY2) and National Severe Storms Laboratory (NSSL) schemes, in the Weather Research and Forecasting (WRF) Model (Skamarock et al. 2008) are examined

due to their improved polarimetric signature accuracy relative to other two-moment BMPs with a single rimed ice category (Johnson et al. 2016). The P3 BMP contains at least one free ice category, which, under appropriate conditions, can represent rimed ice (with a wide range of densities). This study is intended to provide useful information to BMP developers on how to improve microphysical representations and help modelers make educated selections of microphysical schemes for their applications.

The remainder of the paper is organized as follows. Section 2 details the numerical model setup, BMPs, and polarimetric radar data simulator; section 3 analyzes simulated polarimetric variables; section 4 quantifies rimed-ice properties in the BMP schemes; and section 5 summarizes and discusses ramifications of rimed-ice parameterization in supercell simulations.

2. Numerical simulations

a. Model setup

WRF v3.9.1 (Skamarock et al. 2008) is used in this study to produce idealized supercell simulations. The model configuration is similar to Morrison and Milbrandt (2011), and is further detailed in Table 1. Convection is initiated with a thermal bubble with potential temperature perturbation θ' of 3 K on a 200 km \times 200 km grid with horizontal grid spacing of 1 km. The Weisman and Klemp (1982) thermodynamic sounding and a wind profile with a veering “quarter-circle” shear of $3.11 \times 10^{-3} \text{ s}^{-1}$ up to 2.3 km and unidirectional shear of $5.70 \times 10^{-3} \text{ s}^{-1}$ above to 7 km defines the storm’s environment. The model is integrated for 3 h with 6 s time step size using the third-order Runge–Kutta scheme. The domain contains a rigid lid at $z = 20$ km with 40 vertical levels. Rayleigh damping is applied in the top 5 km of the domain, and a 1.5-order turbulent kinetic energy (TKE) scheme is employed for turbulence. As is typical for idealized supercell simulations, we neglect radiation, surface flux, planetary boundary layer, and cumulus parameterizations.

b. Microphysics schemes

Based on the previous study of Johnson et al. (2016) that showed a two-moment BMP with both predefined graupel-like and hail-like rimed ice categories produced a more realistic supercell structure compared to other two-moment schemes with one rimed ice category, this study uses the two-moment Milbrandt–Yau (MY2; to distinguish from the one-moment and three-moment versions of the scheme; Milbrandt and Yau 2005a,b) and National Severe Storms Laboratory (NSSL; Mansell et al. 2010) schemes. The MY2 and NSSL schemes are similar in that

TABLE 1. WRF Model input.

WRF Model configuration	
Run time	180 min
Δt	6 s
Sound wave Δt	1 s
Model output interval	10 min
Horizontal domain	200 km \times 200 km
Model lid	20 km
Δx	1 km
Δy	1 km
Δz	~ 500 m
Time integration scheme	Third-order Runge–Kutta
Horizontal momentum advection	Fifth-order
Vertical momentum advection	Third-order
Horizontal scalar advection	Fifth-order
Vertical scalar advection	Third-order
Upper-level damping	5000 m below model top
Rayleigh damping coefficient	0.003
Turbulence	1.5-order turbulent kinetic energy (TKE)
Horizontal boundary conditions	Open

the mass mixing ratio q_x and total number mixing ratio N_x are prognosed for each hydrometeor category (i.e., cloud water, rain, cloud ice, snow, graupel, and hail). The default MY2 BMP employed here assumes constant densities of 400 and 900 kg m $^{-3}$ for graupel and hail, respectively. Recently, Milbrandt and Morrison (2013) developed a version of the MY2 scheme that prognoses the graupel bulk volume mixing ratio, which allows the graupel density to be predicted; however, this version of the scheme was not available in WRF at the time of this study. The NSSL scheme prognoses both graupel and hail bulk volumes (and hence densities).

This study also uses the Predicted Particle Properties (P3) scheme (Morrison and Milbrandt 2015; Milbrandt and Morrison 2016). The P3 scheme has a similar two-moment two-category representation of the liquid phase as MY2 and NSSL, but has a fundamentally different representation of ice-phase particles, with a user-specified number of “free” ice categories representing all ice particles. For each ice category n , there are four prognostic variables: the total ice mass mixing ratio $q_{i\text{-tot}}(n)$, the rime mass mixing ratio $q_{i\text{-rim}}(n)$, the total number mixing ratio $N_{i\text{-tot}}(n)$, and the rime volume mixing ratio $B_{i\text{-rim}}(n)$, and a complete gamma size distribution describes each category. This specific choice of prognostic variables allows for the smooth evolution of several important physical properties, such as bulk density, size, fall speed, etc. From the specific properties at a given point in time and space, the dominant type of ice particle for a given category can be determined (e.g., lightly rimed aggregate), and this can evolve as the properties change. However, there is no “conversion” from one type

of ice particle to another, as in traditional predefined category schemes like MY2 and NSSL. If the properties of two P3 categories are deemed to be sufficiently similar, based on mean size as a proxy for overall similarity in the current version, ice categories merge into a single category in order to “free up” a category into which new ice can subsequently be initiated. Note that the use of mean size as a proxy for similarity has some utility [see [Milbrandt and Morrison \(2016\)](#)] but is limited; the use of other physical properties (such as bulk density and rime fraction) to determine conditions for merging will be examined in future studies. Even with a single category, the P3 scheme has been shown to be able to simulate realistically a wide range of ice types and performs well for the simulation of deep convective storms and orographic precipitation compared to traditional schemes in WRF ([Morrison et al. 2015](#)).

c. Polarimetric radar data simulator

To facilitate comparisons in BMP rimed-ice parameterization, we compute simulated polarimetric radar variables from WRF model output. The Center for Analysis and Prediction of Storms–Polarimetric Radar data Simulator (CAPS-PRS; [Jung et al. 2008](#); [Jung et al. 2010](#); [Dawson et al. 2014](#)) utilizes precomputed scattering amplitude tables created by the T-matrix method ([Waterman 1969](#); [Vivekanandan et al. 1991](#); [Zhang et al. 2001](#)) that vary with particle diameter, water fraction, and now particle density. The Mie scattering effect is included in scattering calculations. In the two-moment framework of this paper, the CAPS-PRS uses model prognosed q_x and N_{tx} to construct hydrometeor PSDs, with the shape parameter α consistent with microphysical assumptions. The CAPS-PRS calculates snow water fraction following [Jung et al. \(2008\)](#), which also details the axis ratio/canting angle assumptions made by the PRS. The PRS diagnoses rimed-ice water fraction following [Dawson et al. \(2014\)](#). Briefly, rain soaks rimed ice (and freezes) until its density reaches 910 kg m^{-3} , after which subsequent water collects as liquid on the rimed ice hydrometeor. Depending on the particle’s diameter, the wet rimed ice either completely melts or forms a liquid water torus ([Rasmussen and Heymsfield 1987](#)). We note here that water fraction decreases and canting angle standard deviation increases as rimed ice diameter increases [see [Dawson et al. \(2014\)](#) Fig. 2], which allows the PRS to model both stable, small wet rimed ice and tumbling, relatively dry rimed ice. This added water reshapes the distribution, and iterates until the distribution converges. Finally, the PRS calculates horizontal reflectivity Z_H , differential reflectivity Z_{DR} , and cross-correlation coefficient ρ_{HV} from the relevant indexed scattering amplitudes following [Zhang et al. \(2001\)](#) and [Jung et al. \(2010\)](#).

Currently, we neglect cloud water and cloud ice in the CAPS-PRS due to their small sizes.

We list where the CAPS-PRS differs from the above description when calculating P3 scattering amplitudes here. Because P3 microphysics employs a lookup table approach to calculate ice PSD parameters (see [Morrison and Milbrandt 2015](#) for details), we utilize the same approach in the CAPS-PRS. The PRS calculates eight P3 ice PSDs for two rime fractions f_r , rime densities ρ_r , and normalized mass mixing ratios q_i/N_i by using precomputed intercept N_0 , slope Λ , and shape α parameters. These are used to calculate linear polarimetric variables as a function of the simulated rime fraction, rime density, and normalized mass mixing ratio through multidimensional linear interpolation at each grid point. The ice PSDs are appropriately partitioned into m – D relationships (i.e., ice mode) by accessing precomputed critical diameters [we refer the reader to Fig. 1 in [Morrison and Milbrandt \(2015\)](#) for P3 ice property PSD partitions]. Small ice and larger, nonspherical ice from depositional growth and/or aggregation of small ice (which constitutes the smallest ice PSD segments when riming is present) follow Rayleigh scattering and are assumed dry, while fully and partially rimed ice follow the same T-matrix scattering method mentioned above. Water fraction for rimed ice follows [Dawson et al. \(2014\)](#), except without iteration as added water is assumed to not reshape the distribution. The PRS trilinearly interpolates linear horizontal reflectivity Z_h , vertical reflectivity Z_v , and the cross-correlation coefficient numerator Z_{hv} for ice (or water from fully melted ice) calculated for each f_r , ρ_r , and q_i/N_i combination to compute final linear ice polarimetric contributions. The PRS computes P3 rain PSD parameters from model prognosed q_r and N_{tr} through iteration as the rain size distribution shape parameter α is diagnosed from rain slope parameter Λ following [Cao et al. \(2008\)](#). Then, horizontal reflectivity Z_H , differential reflectivity Z_{DR} , and cross-correlation coefficient ρ_{HV} are calculated from their relevant linear components. In this study, all simulated radar variables assume an S-band wavelength (10.7 cm).

3. Simulated supercell radar structure

We examine simulated dual-pol variables at $t = 100$ min, when the supercell has reached a stable, mature state. We note here that the polarimetric supercell signatures examined in this paper are persistent at sampled model times after $t = 100$ min, as they often are in observations (though observed polarimetric signatures are subject to environmental conditions and internal storm dynamics variability that influence signature evolution, such as updraft intensity strengthening a Z_{DR} column, or hail

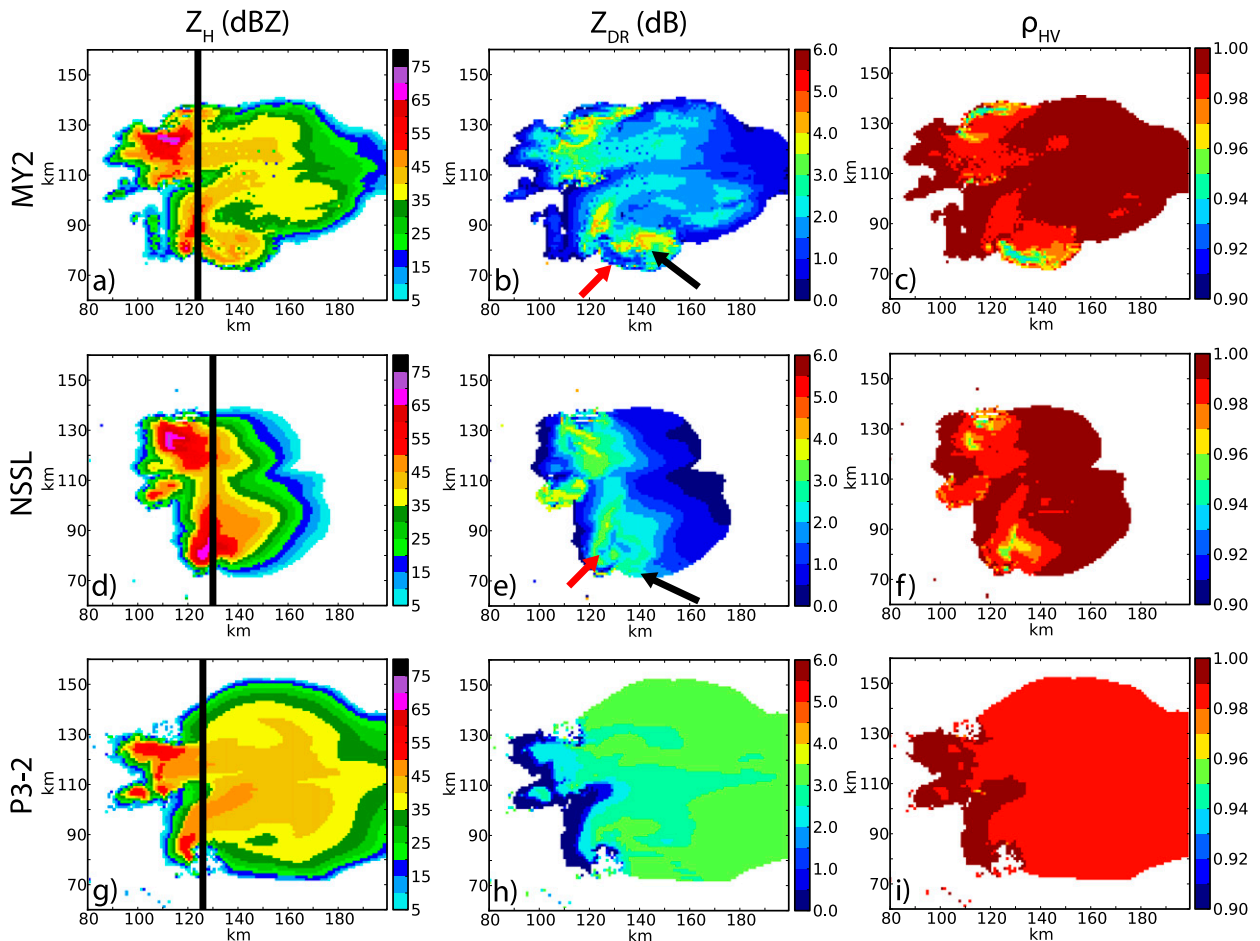


FIG. 1. Horizontal reflectivity Z_H (dBZ), differential reflectivity Z_{DR} (dB), and cross-correlation coefficient ρ_{HV} near $z \approx 280$ m for the (a)–(c) MY2, (d)–(f) NSSL, and (g)–(i) P3–2 microphysics schemes at $t = 100$ min. Vertical black lines in the reflectivity plots denote where vertical cross sections are taken. Black and red arrows in the Z_{DR} subplots denote the simulated Z_{DR} arc and hail signatures, respectively.

disruption of a Z_{DR} arc (e.g., Kumjian and Ryzhkov 2009; Palmer et al. 2011; Van Den Broeke 2016). Because of the veering wind profile, subsequent microphysical analysis focuses on the dominant right-moving cell (e.g., Klemp and Wilhelmson 1978; Rotunno and Klemp 1982; Klemp 1987). The MY2 simulation has somewhat noisy reflectivity (although the melting option used in this paper amplifies reflectivity noise, as wet graupel is not large enough to compensate for the reflectivity reduction due to smaller, melted graupel particles transferring to the rain category as small drops), but the overall structure is well defined (Fig. 1a). Rain, rather than rimed ice, (Figs. 2a, 3a, and 4a) dominates horizontal reflectivity Z_H in the forward flank. Z_H peaks above 60 dBZ in the reflectivity core near the updraft, which is dominated by a small amount (hail mixing ratio $q_h \leq 0.50 \text{ g kg}^{-1}$) of relatively wet (hail water fraction f_{wh} ranging between 0.5 and 1), small to large hail

(hail mass-weighted mean diameter D_{mh} ranging from 4 to 14 mm; Figs. 4a,c,e) rather than graupel (Figs. 3a,c,e). The NSSL scheme produces the smallest forward flank among the three simulations (Fig. 1d), and also the largest reflectivity core, with Z_H exceeding 65 dBZ near the updraft. Large hail ($q_h \geq 0.5 \text{ g kg}^{-1}$, $D_{mh} \geq 14$ mm) in the NSSL scheme with varying degrees of wetness (Figs. 4b,d,f) dominates the reflectivity core over graupel (Figs. 3b,d,f). Z_H in the forward flank follows rain-drop size closer than rain mixing ratio, which in the NSSL BMP at this time typically ranges from low to moderate (rain mass-weighted mean diameter D_{mr} between 0.5 and 3 mm; Figs. 2c,d).

While P3 with one free ice category is highly flexible with ice mode representation, it has the distinct disadvantage that it cannot fully represent different modes of ice particles at the same point in time and space. In the one-category version, the mixing of different

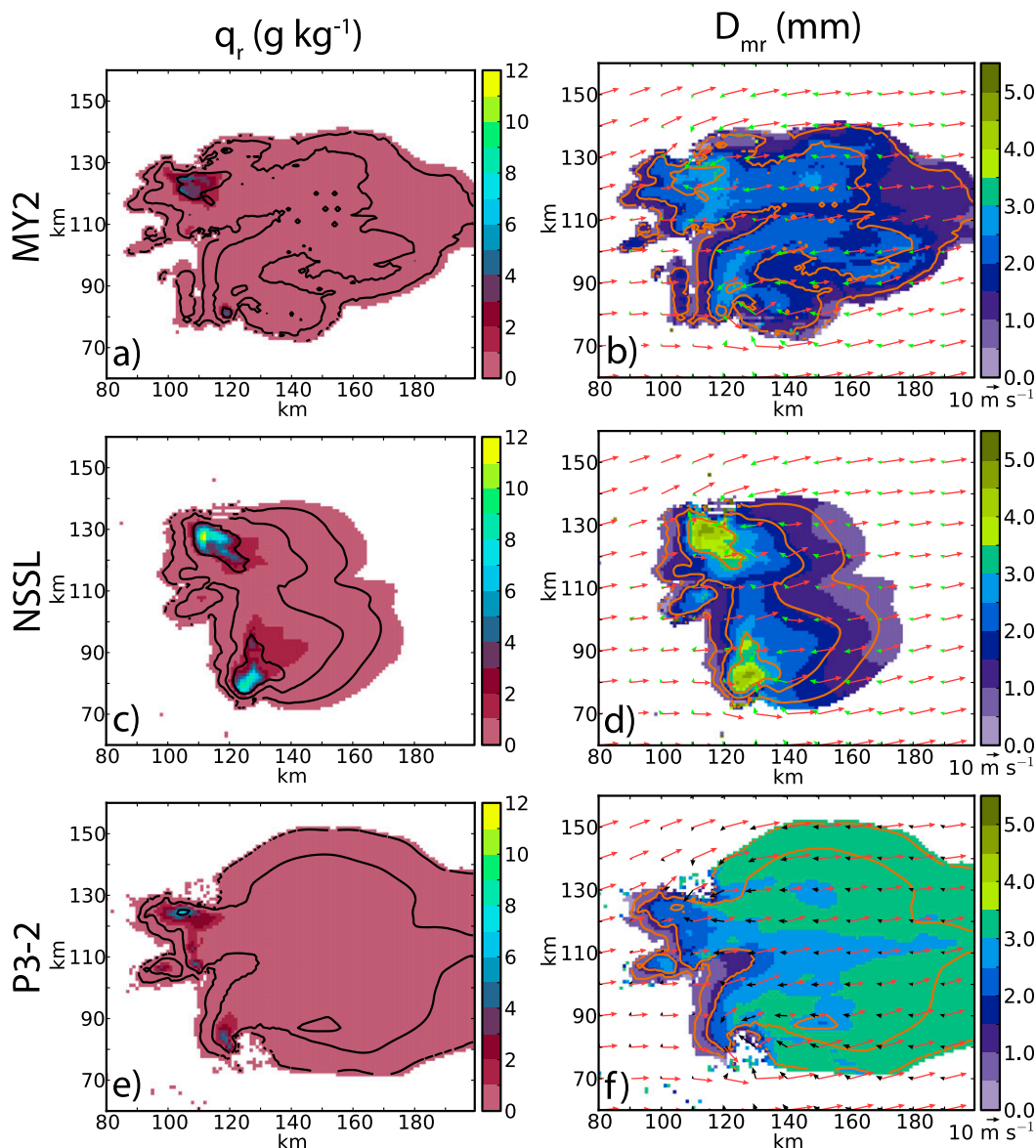


FIG. 2. Rain mixing ratio q_r (g kg^{-1}) and rain mass-weighted mean diameter D_{mr} (mm) near $z \sim 280$ m for the (a),(b) MY2, (c),(d) NSSL, and (e),(f) P3-2 BMPs at $t = 100$ min. Horizontal reflectivity Z_H contours are overlaid in 20 dBZ intervals starting at 15 dBZ. Deep-layer (~ 0.3 – 12 km) and low-level (~ 0.3 – 3 km) storm-relative mean winds are denoted by red and green (black in P3-2) vectors, respectively, in D_{mr} subplots.

populations of ice, for example by differential sedimentation or local initiation of new ice, creates a “dilution” of the physical properties (Milbrandt and Morrison 2016). Although polarimetric variables between P3 with one and two ice categories show qualitative similarity near the surface, we focus on the two ice category configuration of P3 (hereafter referred to as P3-2) to allow for similar degrees of freedom to the other examined BMPs. Also, the P3-2 scheme consistently produces larger mean max (defined in section 4c) ice category 1 diameter in the updraft compared to the

P3 scheme with 1 ice category (not shown), allowing for a higher surface large rimed ice potential. We emphasize that the two free ice categories in P3-2 should not be interpreted as corresponding directly to the two rimed-ice categories in the MY2 and NSSL BMPs; both of the P3-2 ice categories can represent any type of frozen particle. We also point out that comparison of the P3-2 ice categories with MY2 and NSSL BMP rimed ice categories is not a true “apples-to-apples” comparison and caution is needed in comparison. However, we choose to retain the entire P3-2 ice PSDs as the P3

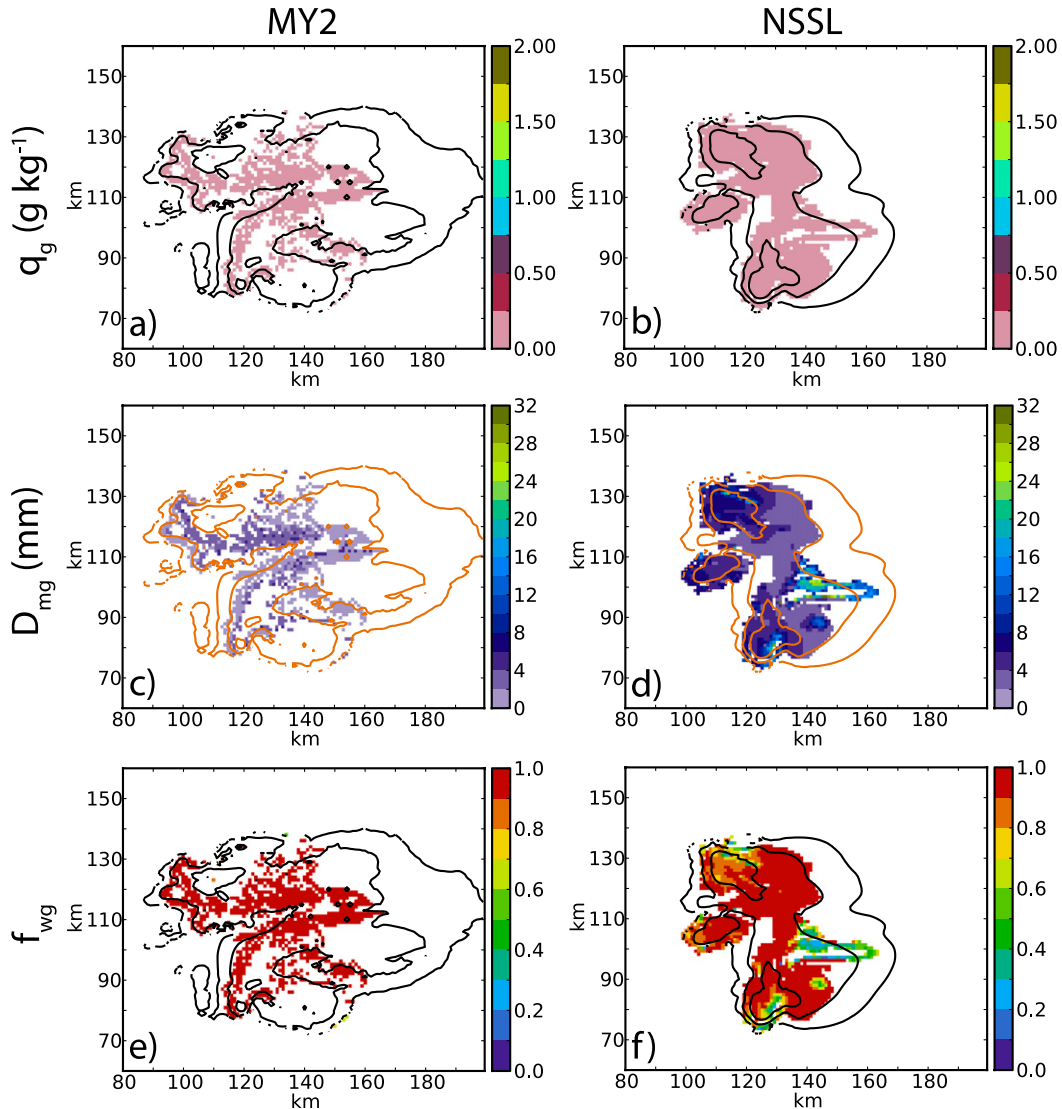


FIG. 3. Graupel mixing ratio q_g (g kg^{-1}), graupel mass-weighted mean diameter D_{mg} (mm), and graupel water fraction f_{wg} near $z = \sim 280$ m for the (a),(c),(e) MY2 and (b),(d),(f) NSSL BMPs at $t = 100$ min. Horizontal reflectivity Z_H contours are overlaid in 20 dBZ intervals starting at 15 dBZ.

scheme segments ice habits on the basis of size and, therefore, analyses including mass-weighted mean diameter D_m , microphysical budgets, and CFADs still provide useful information about rimed ice that occupies the larger-size part of the PSD.

The simulated supercell's forward flank is largest in P3–2 (Fig. 1g). Moderately wet P3–2 (ice category 1 and 2 water fraction $f_{wi,2}$ between 0.4 and 0.6) ice is much smaller (ice category 1 and 2 mass-weighted mean diameter $D_{mi,2} \leq 8$ mm) than MY2 hail and NSSL rimed ice near the surface and is also sparse (ice category 1 and 2 mixing ratios $q_{i,2} \leq 0.25 \text{ g kg}^{-1}$; Fig. 5), subsequently resulting in the weakest reflectivity core among the BMPs examined. We note here that water fraction in

the P3–2 is generally smaller than in the other two BMPs due to the lack of water fraction iteration (when computing water fraction for polarimetric variables as discussed in section 2c) and because we assume not all segments of P3–2 ice PSDs are wet. Rain in the scheme easily dominates ice's contribution to reflectivity, which is larger in the forward flank (D_{mr} exceeds 3 mm) than the other two BMPs (Figs. 2e,f). Consequently, Z_H exceeds 40 dBZ in the forward flank over a greater area compared to the other BMPs. Near the surface, few differences arise between the two ice categories in P3–2. Mixing ratio, mean particle size, and water fraction are very similar between the two categories. The first category (hereafter iceCat 1) is more abundant

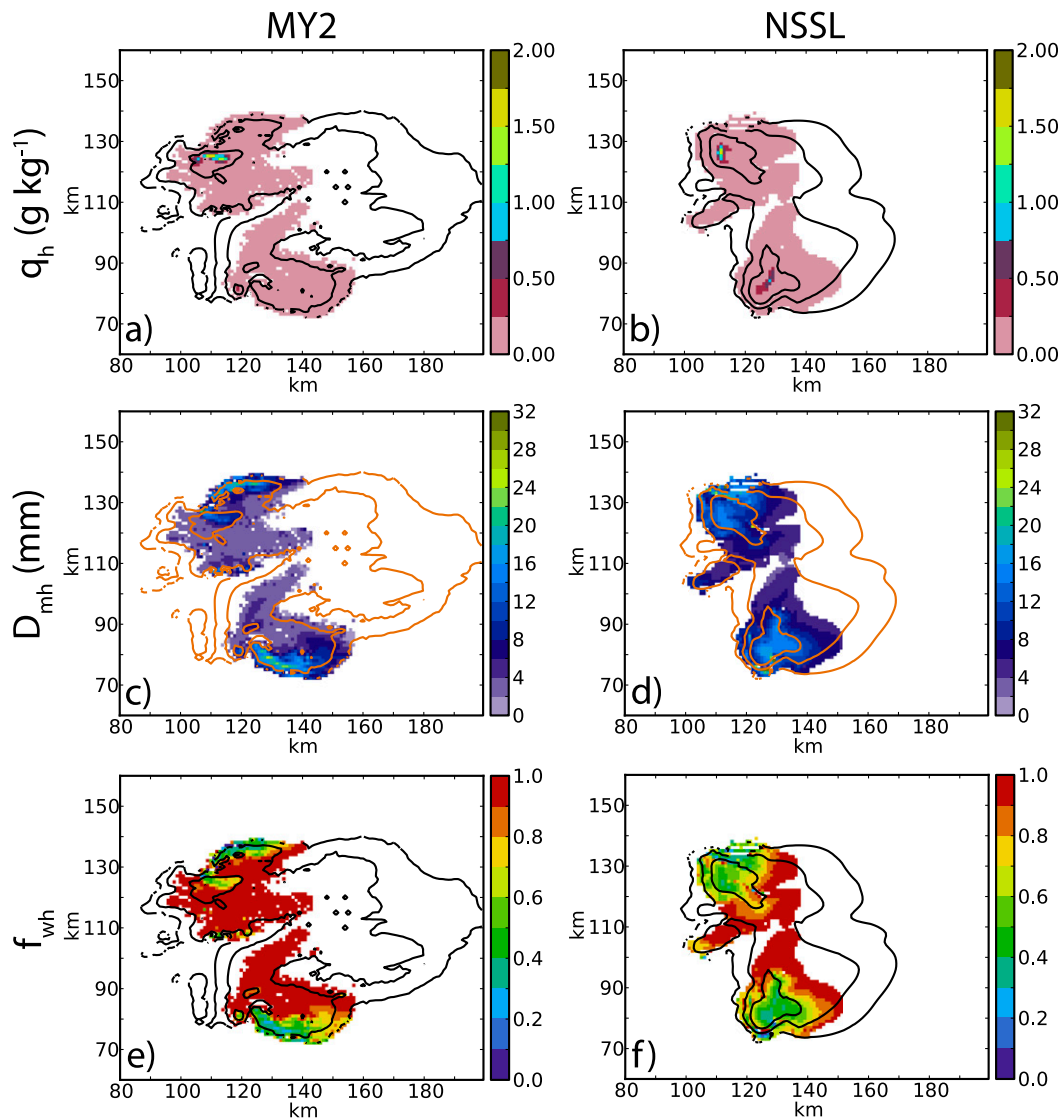


FIG. 4. As in Fig. 3, but for hail.

spatially than the second category (hereafter iceCat 2) because iceCat 2 is always merged with iceCat 1 when the differences in their mass-weighted mean diameters are within 0.5 mm.

a. Z_{DR} arc

Observationally, the size sorting of hydrometeors results in a local Z_{DR} maximum on the southern flank of the right-moving storm called the Z_{DR} arc. Ryzhkov et al. (2005) and Kumjian and Ryzhkov (2008, 2009) primarily attributed this Z_{DR} maximum to large, oblate raindrops. Through numerical simulations, Dawson et al. (2014) showed that simulated Z_{DR} arcs are potentially more influenced by the size sorting of rimed ice rather than rain (given rimed ice's greater sedimentation

depth and additionally providing rain's spatial pattern near the melting level), and Dawson et al. (2015) clarified that storm-relative winds are the kinematic driver of size sorting. Large rimed ice exiting the updraft will fall to the surface faster than smaller rimed ice particles, and therefore, will be less prone to horizontal advection by storm-relative winds. Therefore, a gradient of large to small rimed ice particles will form in the direction of the deep-layer storm-relative mean wind vector [~ 0.7 – 12 km in Dawson et al. (2014) simulations]. The low-level storm-relative mean wind vector [~ 0.7 – 3 km in Dawson et al. (2014) simulations] modulates the horizontal spatial distribution of rain hydrometeors (as low-level storm-relative mean winds are implicitly present in the deep-layer storm-relative mean winds responsible for rimed

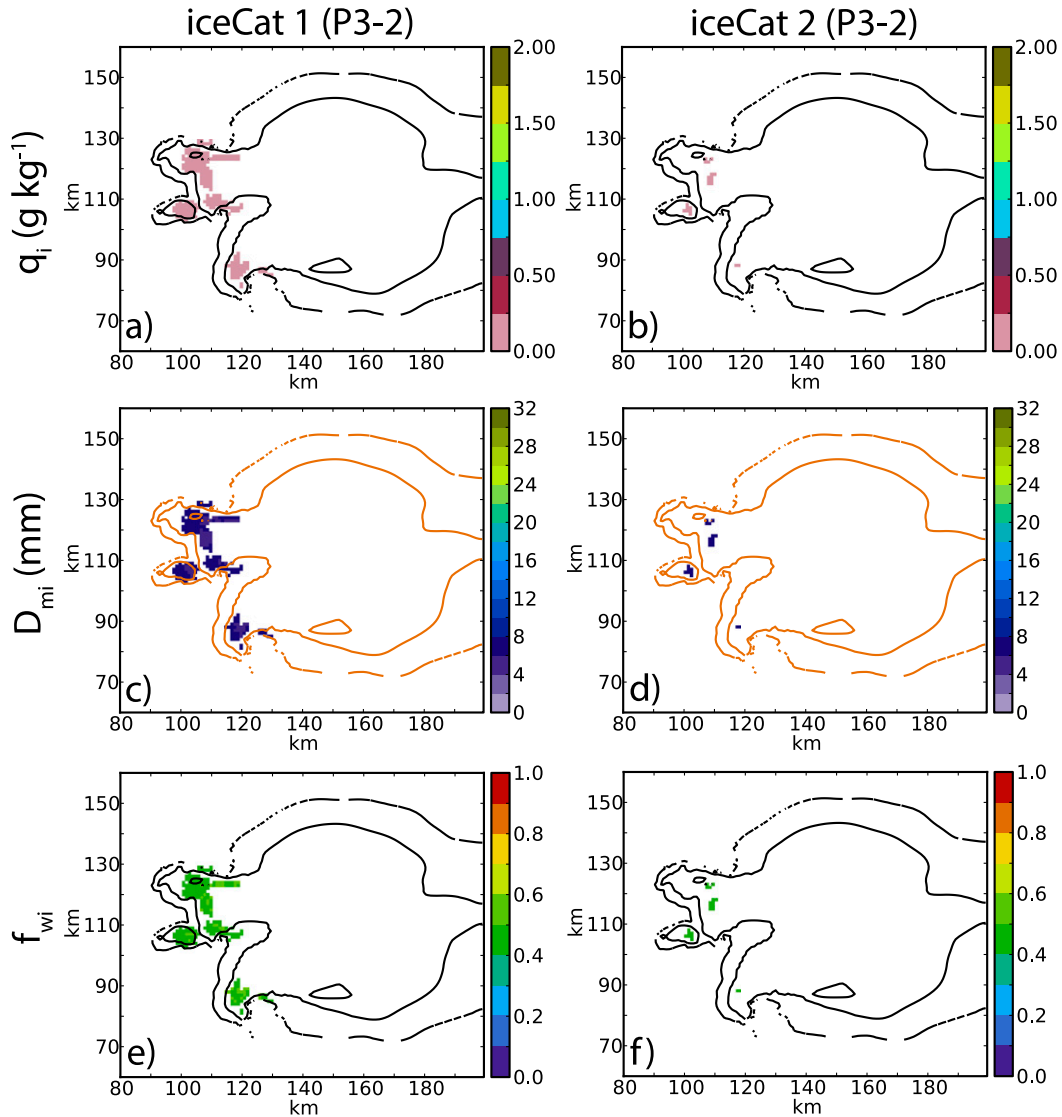


FIG. 5. Ice mixing ratio q_i (g kg^{-1}), mass-weighted mean diameter D_{mi} (mm), and ice water fraction f_{wi} near $z = \sim 280$ m for ice category (a),(c),(e) 1 and (b),(d),(f) 2 in the P3-2 BMP at $t = 100$ min. Horizontal reflectivity Z_H contours are overlaid in 20 dBZ intervals starting at 15 dBZ.

ice size sorting) in its direction, but since this layer is shallower than the deep layer, it has a smaller impact on the final surface distribution of hydrometeors (Dawson et al. 2014). In our simulations, the deep-layer (~ 0.3 – 12 km) storm-relative mean wind (typically southwesterly, but also northwesterly near the tip of the supercell's hook; Figs. 2b,d,f) advects hydrometeors to the east of the updraft (both north and south), the horizontal extent of which is determined by particle size. Low-level storm-relative mean winds in our simulations (~ 0.3 – 3 km) are typically north- or southeasterly, which advects particles to the west and shortens the eastern extent of rain hydrometeors at the surface. Therefore, the expected size sorting and resultant surface hydrometeor distributions

are as follows: large drops from melted rimed ice and large (dry and partially wet) rimed ice in our simulations with westerly momentum quickly fall out to the east of the updraft. Increasingly smaller particles are expected to advect farther to the northeast of the southern flank and create a hydrometeor size gradient that is largest near the southern flank and decreases in the direction of the deep-layer storm-relative mean wind vector (while the surface raindrop size gradient is modulated to the west by the low-level storm-relative wind vector).

Similar to Johnson et al. (2016), both the MY2 and NSSL schemes exhibit clear signs of size sorting in the general direction of the deep-layer storm-relative mean wind vector (Figs. 1b,e). However, each BMP's

simulated Z_{DR} arc exhibits its own shortcomings. The MY2 scheme simulates an elongated region of high Z_{DR} exceeding 4 dB, and is primarily due to wet hail (and oblate raindrops from melted hail following the water fraction diagnostic method employed in this paper; Figs. 4a,c,e). Z_{DR} on the southern edge of the supercell is low (≤ 1.5 dB) and is due to large (D_{mh} exceeding 14 mm), relatively dry (f_{wh} below 0.5) hail in the scheme (Figs. 4c,e). Z_{DR} is also unexpectedly enhanced to the north of the updraft, due to oblate wet hail and rain in this area. The NSSL BMP shows a clear Z_{DR} decrease from the southern flank of the supercell into the forward flank to the northeast. This Z_{DR} arc is simulated from oblate rain (Fig. 2d) and wet hail in this region (Figs. 4b,d,f). However, the horizontal extent and intensity of the Z_{DR} arc are underpredicted. The D_{mr} field in the P3–2 BMP is nearly homogenous near the surface where rain is the dominant hydrometeor (Fig. 2f). Therefore, a Z_{DR} arc is not seen in Fig. 1h as the Z_{DR} field in the forward flank follows the D_{mr} field, although raindrop size does decrease to the west on the western flank of the storm, consistent with the low-level winds and rain size sorting in Dawson et al. (2014). Z_{DR} in the P3–2's forward flank is much larger (≥ 2.5 dB) than the other two schemes, a result of D_{mr} exceeding 3 mm in large areas.

As a major source of large raindrops is melting rimed ice, we consider horizontal ice and rimed-ice mass-weighted mean diameter plots near $z = \sim 4.5$ km (Fig. 6) to examine the impact of rimed ice melting on rain size sorting near the surface. $z = \sim 4.5$ km is chosen because the melting layer is primarily near $z = \sim 4$ km, as shown in later vertical cross sections (Fig. 7). P3–2 ice plots are shown because the rime fraction f_r is typically above 0.8. Graupel in MY2 displays a size maximum ($D_{mg} \geq 4$ mm) in the middle of the storm, away from the updraft (Fig. 6a). Larger hail ($D_{mh} \geq 10$ mm) in the scheme produces a more distinct size sorting distribution, with large particles on the southern edge of the right-moving cell and hail size decreasing into the forward flank to the northeast (Fig. 6b). MY2 hail also displays enhanced hail sizes advected to the north of the updraft (consistent with deep-layer storm-relative mean winds), likely providing the source of the unexpected surface Z_{DR} enhancement to the north of the supercell's updraft. In NSSL, both graupel and hail ($D_m \geq 10$ mm, which is larger than MY2 graupel) display larger particles near the updraft, where rimed ice initiates and grows (Figs. 6c,d). The large difference in graupel distribution between the MY2 and NSSL schemes is partly due to different assumptions for graupel. NSSL graupel spans a greater rimed ice property range (i.e., continuous riming growth to hail through prognostic bulk volume), while MY2 graupel is more constrained as a smaller,

medium-density rimed ice category (and has a relatively flat graupel fall speed curve that is typically slower than NSSL graupel fall speed [not shown], which allows for greater MY2 graupel horizontal advection into the forward flank). We also note that MY2 hail has a smaller horizontally averaged mass-weighted mean fall speed than NSSL hail over the depth of the model domain, allowing for a greater downstream advection from the updraft by storm-relative winds (which are more northerly in this area in MY2, likely dictated by microphysical feedback to ambient thermodynamics [e.g., latent heat and buoyancy] as each simulation initiates with the same shear profile; Fig. 2b). The greater downstream advection of MY2 hail is less expected compared to the faster falling NSSL hail that remains closer to its updraft source. Though MY2 graupel size sorting is weak (D_{mg} maxima in the center of the storm that decreases away), both the MY2 and NSSL schemes display rimed ice size sorting as D_m decreases to the northeast of the storm, an important precursor for simulated supercell low-level Z_{DR} arcs and their associated gradient in the direction of the storm-relative winds (e.g., Dawson et al. 2014).

The mass-weighted mean diameter of iceCat 1, D_{mi1} , exhibits evidence of size sorting as particle size increases toward the edges of the storm (Fig. 6e). Maximum ice size is smaller in P3–2 than in the other schemes (except for MY2 graupel), resulting in a weaker gradient. Similar to MY2 hail, the typically smaller horizontally averaged mass-weighted mean fall speed of P3–2 iceCat 1 compared to NSSL hail allows for greater downstream advection from the updraft by storm-relative winds (which are more northerly in this area than in the NSSL simulated storm, again likely dictated by P3 BMP microphysical feedback to its surrounding environment; Fig. 2f). Further, D_{mi2} in P3–2 depicts a rather noisy pattern with size generally increasing toward the middle of the splitting storm (Fig. 6f). The spatial pattern of iceCat 2 should not affect the rain distribution near the surface, as the mixing ratio of iceCat 2 is typically smaller than that of iceCat 1 (not shown). Although the predefined rimed-ice categories in the MY2 and NSSL schemes are fundamentally different from those in P3–2, comparison to these predefined schemes can help ensure that BMPs with more ice mode flexibility indeed improve the representation of the wide range of ice modes. The striking differences in midlevel ice distributions between the P3–2 and other BMPs suggest that some processes related to ice size sorting may need improvement in P3.

b. Hail signature in forward-flank downdraft (FFD)

Dry, large hailstones tumble during sedimentation, appearing spherical to radar and substantially reducing observed Z_{DR} typically downstream in close proximity

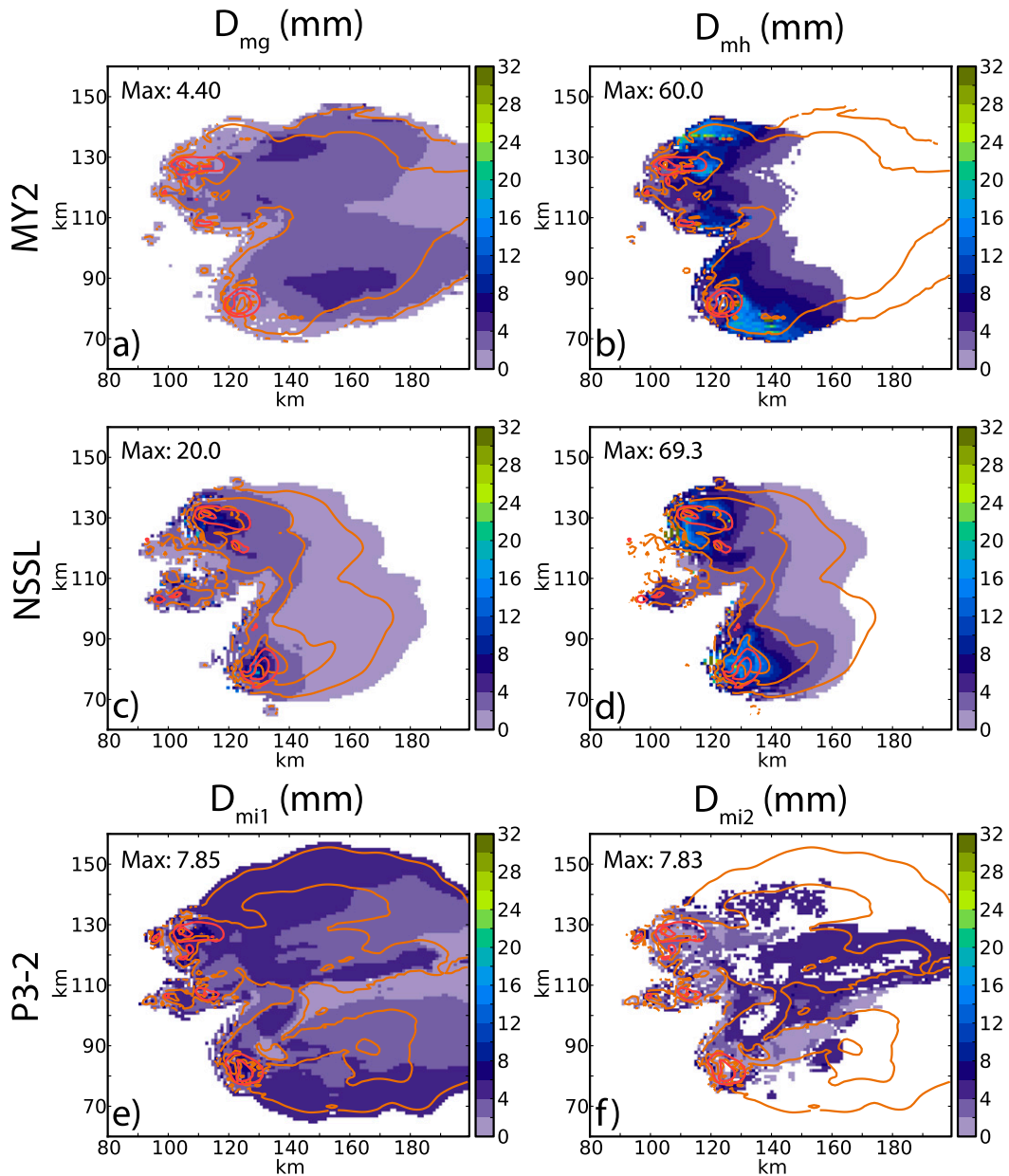


FIG. 6. Mass-weighted mean diameter of graupel D_{mg} (mm) and hail D_{mh} (mm) near $z = \sim 4.5$ km for the (a),(b) MY2 and (c),(d) NSSL BMPs and ice category 1 D_{mi1} (mm) and 2 D_{mi2} (mm) near $z = \sim 4.5$ km for the (e),(f) P3-2 scheme at $t = 100$ min. Included in each panel is the maximum D_m . Orange horizontal reflectivity Z_H contours are overlaid in 20 dBZ intervals starting at 15 dBZ, while red contours are vertical velocity with 15 m s^{-1} interval starting at 10 m s^{-1} .

of the supercell’s updraft (Kumjian and Ryzhkov 2008). As rimed ice canting angle standard deviation increases linearly with decreasing water fraction in the polarimetric simulator employed in this study, simulated rimed ice does not need to be completely dry to reduce Z_{DR} . Another consequence of this parameterization is that the tumbling rimed ice that reduces Z_{DR} may also reduce ρ_{HV} due to the resonance effect in the

Mie scattering regime (Kumjian and Ryzhkov 2008, 2009; Jung et al. 2010), and is accounted for in the scattering amplitudes constructed by the CAPS-PRS using the T-matrix method. Therefore, an area of reduced ρ_{HV} overlapping reduced Z_{DR} can be reasonably attributed to rimed ice in the supercell framework of this study.

Near the surface in the MY2 scheme, large, relatively dry hail (D_{mh} exceeding 14 mm, f_{wh} below 0.5; Figs. 4c,e)

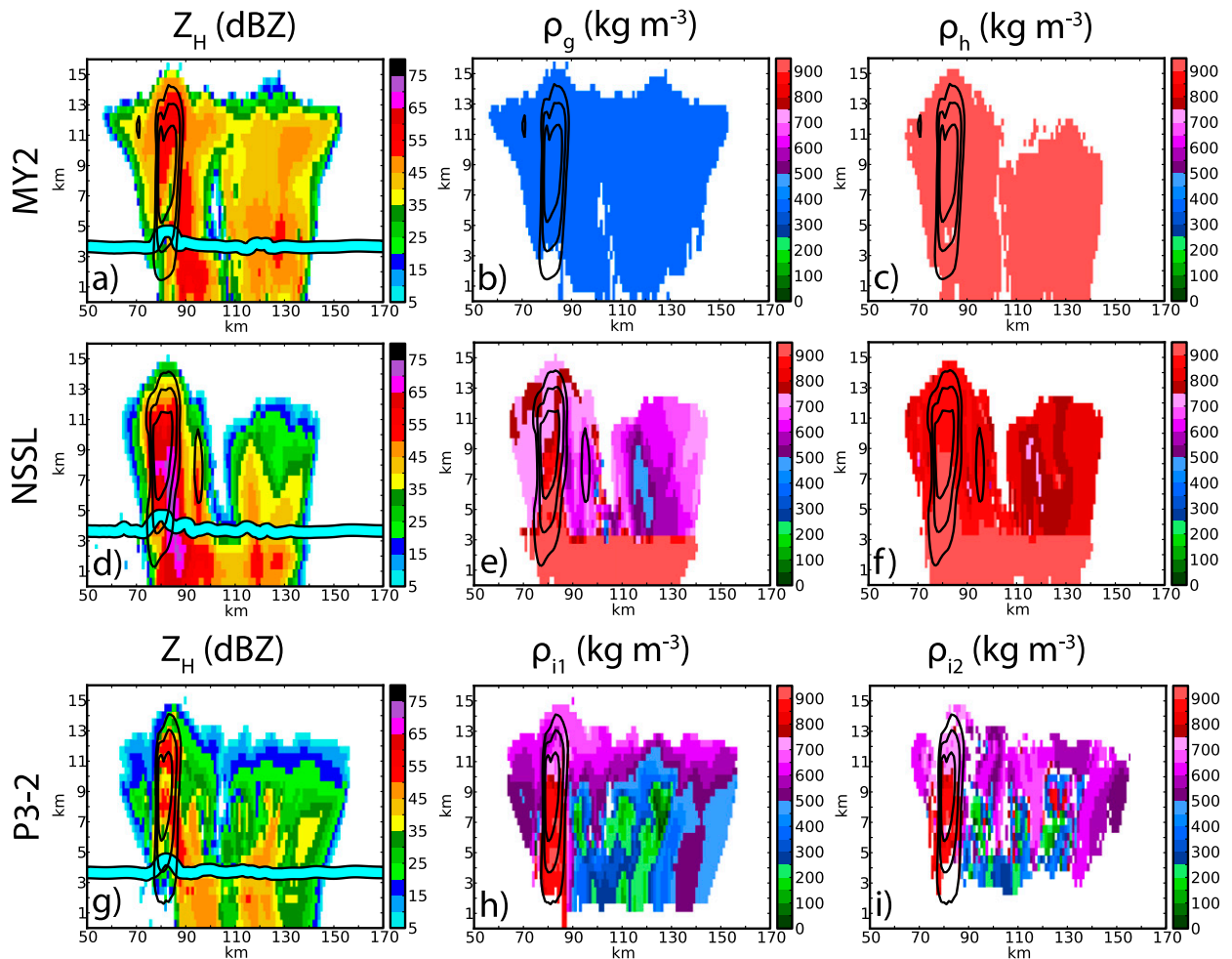


FIG. 7. Horizontal reflectivity Z_H (dBZ), graupel bulk density ρ_g (kg m^{-3}), and hail bulk density ρ_h (kg m^{-3}) for the (a)–(c) MY2 and (d)–(f) NSSL schemes, and Z_H (dBZ) and ice bulk density for ice categories 1 ρ_{i1} (kg m^{-3}) and 2 ρ_{i2} (kg m^{-3}) in the (g)–(i) P3–2 scheme through the updraft at $t = 100$ min. The melting level is depicted as a 0°C isotherm blue line, and vertical velocity contours are shown with 15 m s^{-1} interval starting at 10 m s^{-1} .

reduces Z_{DR} substantially and ρ_{HV} (as the hail particles are mixed-phase) below 0.94 (Figs. 1b,c). However, the location of the MY2 Z_{DR} reduction is extended too far south into the southern flank compared to typical hail signature observations (Kumjian and Ryzhkov 2008). The MY2 Z_{DR} reduction span and location is likely due to a smaller mass-weighted mean hail fall speed over the deep layer (~ 0.3 – 12 km) compared to the NSSL scheme (not shown), which would allow MY2 hail to advect further to the right of the updraft following the deep-layer storm-relative wind, rather than quickly falling out close to the updraft. In the NSSL scheme, large, relatively dry hail ($D_{\text{mh}} \geq 12$ mm, f_{wh} below 0.5) reaches the surface (Figs. 4d,f) and reduces Z_{DR} closer to the typically observed signature (i.e., immediately downstream of the updraft) than the MY2 (Fig. 1e). We note that this dry hail also offsets the large Z_{DR}

contribution by the most oblate rain near the surface (to the northwest of the right flank; Fig. 2d), as hail is assumed to not collect rain in the NSSL scheme where ambient temperature exceeds 0°C . The Z_{DR} reduction is additionally not as much as the hail signature produced in Johnson et al. (2016). These hail signature differences underscore how different BMP versions can manifest themselves in simulated polarimetric signatures. Hail in the NSSL scheme also reduces ρ_{HV} in the same location as the Z_{DR} reduction below 0.96 (Fig. 1f), which is a smaller ρ_{HV} reduction than in the MY2 scheme. Hail is larger in the MY2 scheme in this reduced ρ_{HV} region and consequently contains more particles prone to the resonance effect than NSSL hail.

In P3–2, ice barely reaches the surface and there is no simulated Z_{DR} reduction from large dry rimed ice (Fig. 1h). Ice is only present in small quantities near the

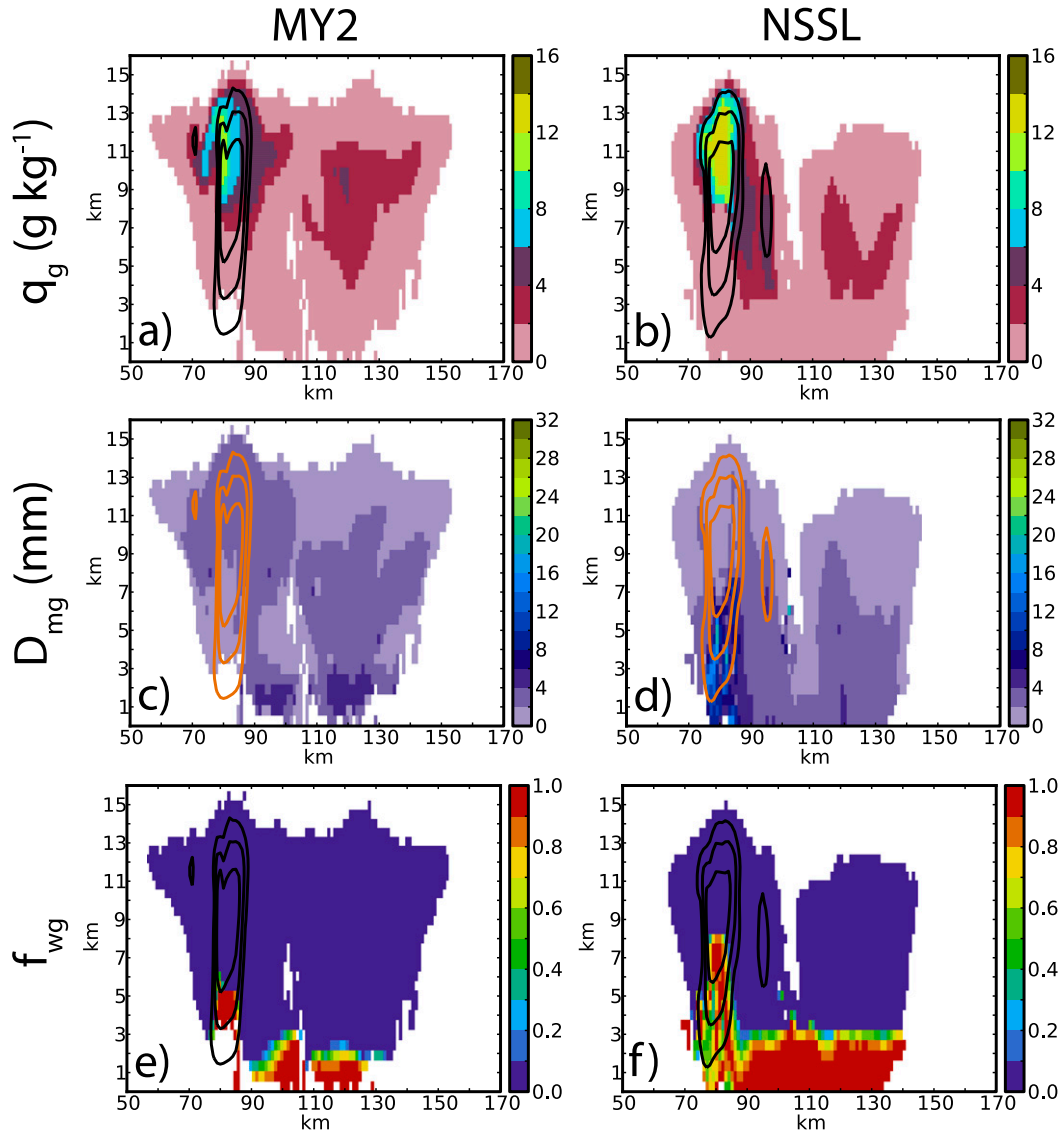


FIG. 8. Graupel mixing ratio q_g (g kg^{-1}), graupel mass-weighted mean diameter D_{mg} (mm), and graupel water fraction f_{wg} through the updraft for the (a),(c),(e) MY2 and (b),(d),(f) NSSL BMPs at $t = 100$ min. Vertical velocity contours are shown with 15 m s^{-1} interval starting at 10 m s^{-1} .

supercell's hook appendage ($q_{i1,2} \leq 0.25 \text{ g kg}^{-1}$; Fig. 5), and iceCat1's relatively small ($D_{mi1} \leq 8 \text{ mm}$) and moderately wet (f_{wi1} between 0.4 and 0.6) ice particles actually increase Z_{DR} where present. This is primarily due to the scheme's restrictive maximum ice number-weighted mean diameter D_{ni} limit, which prevents the growth of large ice. We emphasize here that the maximum D_{ni} limit in this paper is only examined as a tuning parameter, which will be discussed later; it is not a PSD characteristic, unlike the mass-weighted mean diameter D_m . Based on its water fraction f_{wi} , ice in the P3-2 scheme is mixed-phase and therefore has the potential to reduce ρ_{HV} near the surface. However, ρ_{HV} near the

surface is generally large (≥ 0.98 ; Fig. 1i), as wet ice particles in the P3-2 scheme are much smaller than hail in the MY2 and NSSL schemes, and therefore are less prone to the resonance effect. In fact, much of the ρ_{HV} reduction in the P3-2 scheme is due to relatively medium-sized, oblate drops ($D_{mr} \geq 2.5 \text{ mm}$; Fig. 2f).

c. Updraft hail core

We analyze vertical cross sections through the updraft to examine vertical distributions of rimed ice (Fig. 7). Upper-level Z_H in MY2 peaks high in the updraft, near $z = 12 \text{ km}$ (Fig. 7a). While dry graupel is prominent in this area (Figs. 8a,e), it is also relatively

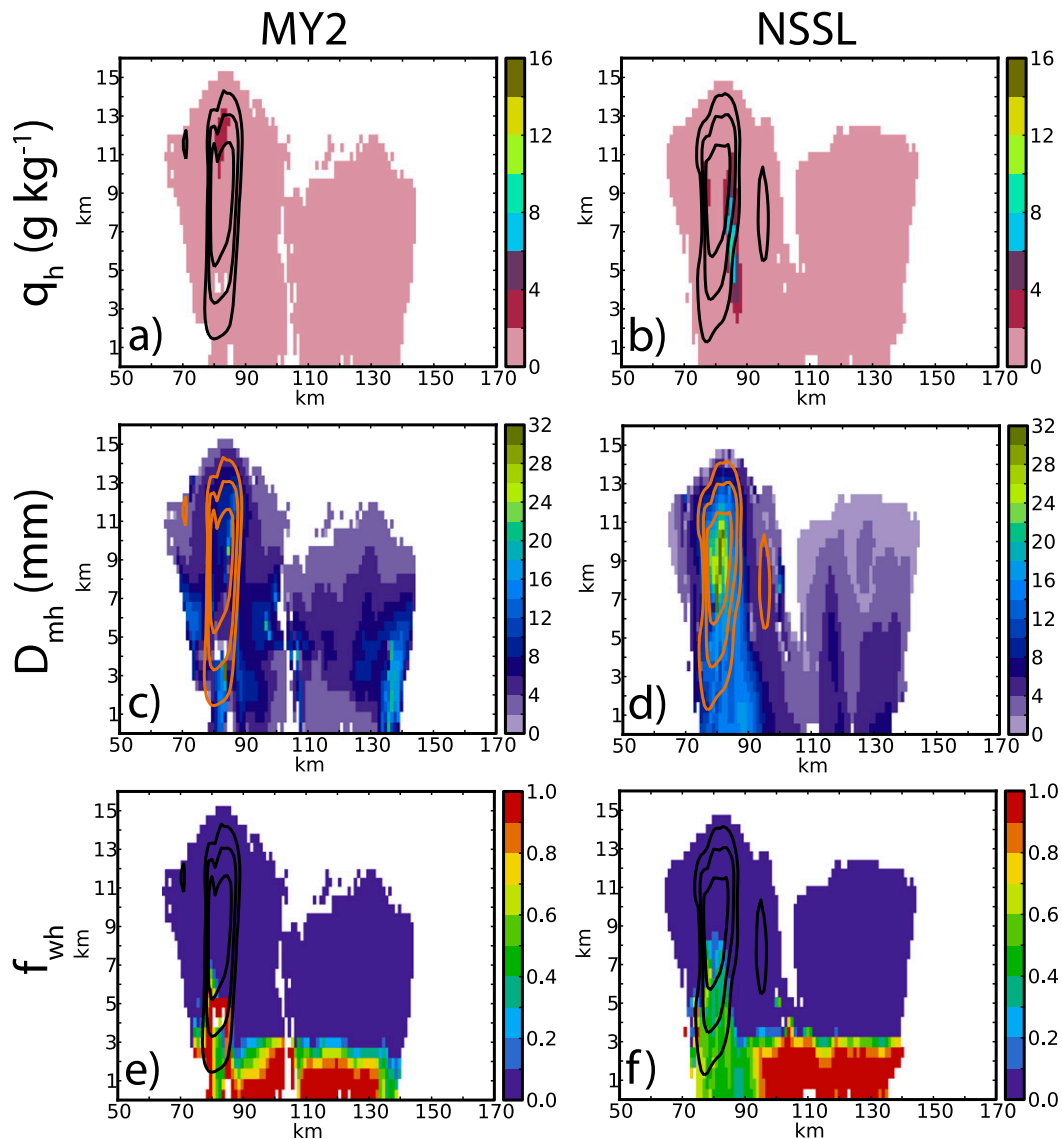


FIG. 9. As in Fig. 8, but for hail.

small ($D_{mg} \leq 4$ mm; Fig. 8c). Therefore, a small amount (q_h between 0 and 4 g kg^{-1}) of relatively moderate, dry hail ($D_{mh} \geq 8$ mm, $f_{wh} \leq 0.1$; Figs. 9a,c,e) is responsible for the enhanced Z_H . Z_H in the NSSL scheme peaks lower in the updraft, below $z = 8.5$ km (Fig. 7d) on the northern edge of the updraft. Low amounts (q_g typically below 6 g kg^{-1}) of graupel with a sharp water fraction gradient (Figs. 8b,d,f) in this area are smaller than moderate amounts (max q_h of 10 g kg^{-1}) of both dry and wet hail in the area (f_{wh} between 0 and 0.6; Figs. 9b,d,f). The largest hail produced in the NSSL scheme ($D_{mh} \geq 30$ mm) does not correlate with the Z_H maximum, which is mainly due to lower q_h (typically less than 2 g kg^{-1}) and water fraction (drier; typically less than 0.2). Included in the reflectivity figures are rimed-ice densities,

which are constant in MY2 (Figs. 7b,c) and predicted in NSSL (Figs. 7e,f). In the NSSL scheme, graupel and hail densities are both large (generally above 700 kg m^{-3}) and similar in the updraft and below the melting level, indicative of the NSSL scheme's hail source requiring sufficient graupel wet growth (i.e., riming) and facilitated through the scheme's graupel (and hail) prognostic bulk volume. This rimed ice philosophy also explains graupel's larger density range compared to hail over the supercell. Compared to the prescribed constant density values in the MY2 scheme of 400 and 900 kg m^{-3} for graupel and hail, respectively, NSSL graupel density is typically larger while hail density is slightly smaller, reflective of the NSSL BMP's predicted rimed-ice bulk volume simulating wet growth in a smooth, continuous manner.

The P3–2 scheme produces two distinct Z_H maxima within the updraft, one near $z = 12$ km and one below $z = 9.5$ km (Fig. 7g). While the upper-level maximum is primarily caused by moderate amounts (q_{i1} generally between 4 and 10 g kg^{-1}) of relatively large, dry ($f_{wi1} \leq 0.1$) iceCat 1 (Figs. 10a,c,e), dry iceCat 2 is prominent where iceCat 1 reduces to a local minimum (Figs. 10b,d,f). The iceCat 1 and 2 juxtaposition near $z = 12$ km helps illustrate P3 ice category interaction, as both categories initiate, grow independently of each other, and are kept separate as long as they are not similar in size. The combination of the two separate categories helps produce a smooth, continuous reflectivity field, while the individual ice categories themselves can become noisy. The Z_H maximum below $z = 9.5$ km and extending to 3 km is predominantly caused by both moderately dry and wet iceCat 1 (f_{wi1} between 0 and 0.5), though iceCat 2 also contributes to this maximum. The mass-weighted mean diameters of both iceCat1 and iceCat2 are typically smaller ($D_{mi,2} \leq 8$ mm) than MY2 and NSSL hail in the updraft, but the P3–2 has a reflectivity core similar in magnitude to the MY2. While P3–2 typically produces more mass than MY2 hail in the upper Z_H maximum, it is also important to remember that P3–2 ice mass-weighted mean diameter spans the entire PSD, including smaller nonrimed ice. In P3–2, bulk densities (which include small spherical and large nonspherical ice) are generally very similar between the two ice categories (Figs. 7h,i). Bulk density is largest (generally above 500 kg m^{-3}) in the updraft where riming processes dominate, and decreases farther away. Though P3 ice categories are not exclusively rimed ice, rime fraction f_r is typically greater than 0.8 in the vertical cross section (Figs. 10g,h) indicating the dominance of riming growth over vapor deposition. For medium-large densities (i.e., $\rho_i \geq 500 \text{ kg m}^{-3}$) in the updraft and near the top of the supercell, the majority of the ice PSD is rimed and partially rimed ice, similar to the graupel and hail predefined categories in the MY2 and NSSL BMPs. Small spherical and large nonspherical ice become more prominent away from the updraft as density and rime fraction decrease.

4. Rimed-ice properties

a. Microphysical tendencies

To understand better the production and depletion of rimed ice, we analyze average mixing ratio q_x and number concentration N_x tendencies in the MY2 and NSSL schemes, and both free ice categories in the P3–2 scheme at $t = 100$ min (Figs. 11 and 12). We sum the tendencies over 5 min at each grid point, and then over the horizontal domain at each model height level.

The 5-min processes are normalized by the number of seconds over this period to produce average tendencies. Tendencies are only included in Figs. 11 and 12 if the maximum average tendencies (which are horizontally and temporally summed before normalization) that vary with height exceed q and N_t tendency thresholds of $0.25 \text{ g kg}^{-1} \text{ s}^{-1}$ and $1 \text{ m}^{-3} \text{ s}^{-1}$, respectively, to limit discussion to tendencies that contribute most to these bulk quantities. The naming convention for the microphysical processes is based on Milbrandt and Yau (2005b). The first letter denotes the relevant bulk quantity related to the tendency (Q for mixing ratio, N for number concentration). The next two letters denote the process itself (CL: collection, MG: merging, ML: melting, CN: conversion, VD: vapor deposition, SH: shedding, FZ: freezing, VS: vapor sublimation, NC: nucleation, SP: splintering). The last two letters indicate the hydrometeor sink and source, respectively (V: vapor, R: rain, C: cloud water, I: cloud ice, S: snow, G: graupel, H: hail, I1: P3–2 ice category 1, I2: P3–2 ice category 2). The exception to this notation is 3-component freezing, which sums all tendencies (e.g., all liquid-ice freezing to rimed ice in the microphysics schemes) that contribute to this process. A description of each microphysical process examined is available in Table 2.

Three-component freezing primarily initiates MY2 graupel right above the freezing level, while graupel collecting cloud water provides the largest source of q_g between $z = 6$ – 10 km (Figs. 11a,b). The three-component freezing of water and graupel in the MY2 scheme can either go to graupel or hail, which is why the scheme has both source (3compqg-R) and sink (3compqg-K) terms. On the other hand, NSSL graupel primarily initiates from freezing rain (Figs. 11e,f). This reveals a subtle graupel initiation difference between the MY2 and NSSL BMPs for these idealized supercell simulations, as MY2 graupel prefers an ice seed when freezing water to graupel while NSSL graupel does not. Similar to the MY2 scheme, NSSL graupel grows by collecting liquid mass (cloud water and rain), which is expected given the convective updraft in the supercell. Hail converting to graupel (which is an artificial process, present only for optimization) provides a larger source of graupel number aloft in the MY2 scheme and below the melting level but not mass, which is expected as only small hail converts to graupel (hail mean mass diameter $D_h < 1$ mm). This process is not present in the default NSSL scheme, as NSSL hail is designed to primarily originate from larger and heavily rimed graupel. Melting provides a large sink of graupel below the melting level in both the MY2 and NSSL schemes, although it is more aggressive in the NSSL scheme. The three-component freezing provides a large graupel number sink above the

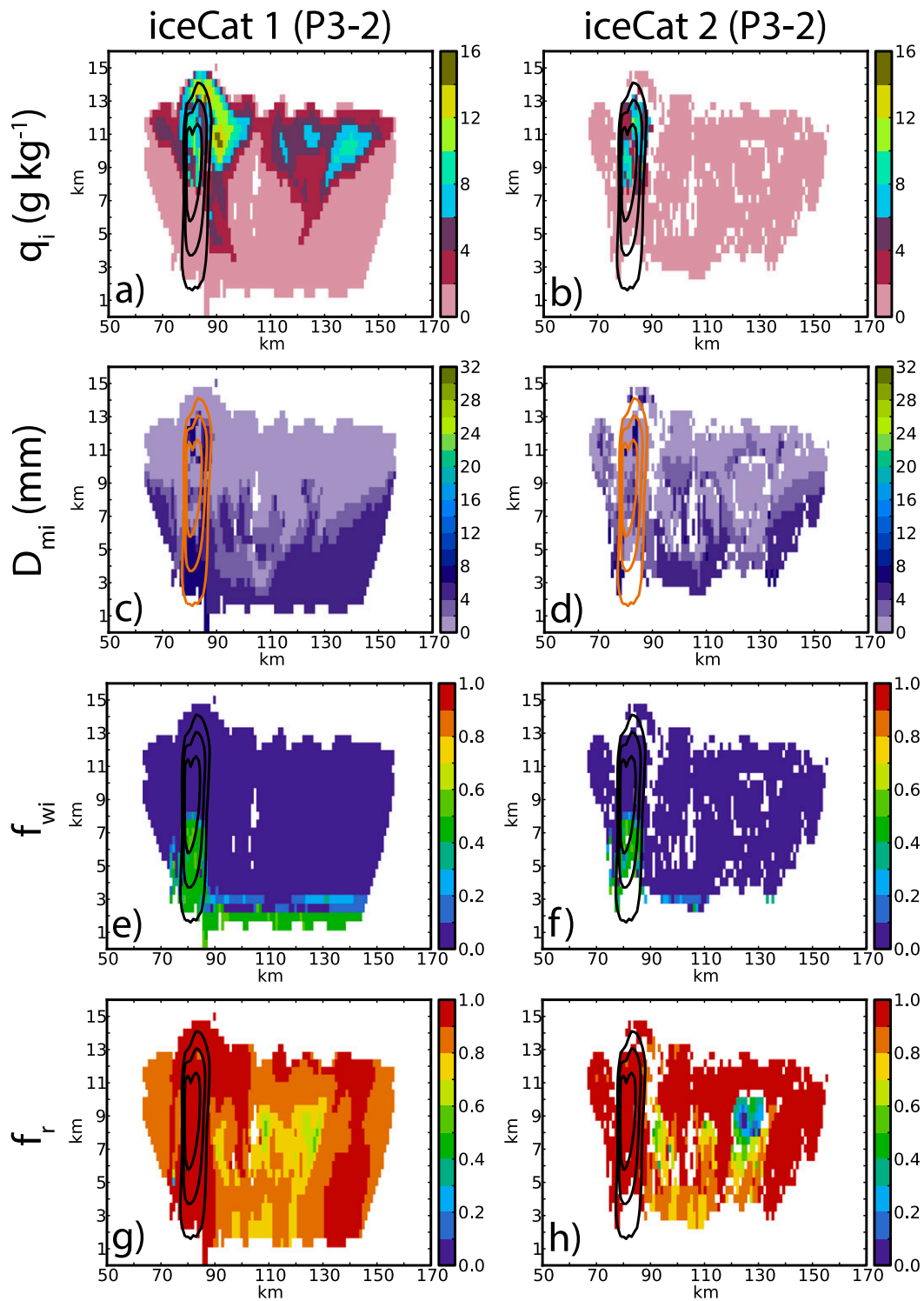


FIG. 10. Ice mixing ratio q_i (g kg^{-1}), mass-weighted mean diameter D_{mi} (mm), ice water fraction f_{wi} , and rime fraction f_r through the updraft for ice category (a),(c),(e),(g) 1 and (b),(d),(f),(h) 2 in the P3-2 BMP at $t = 100 \text{ min}$. Vertical velocity contours are shown with 15 m s^{-1} interval starting at 10 m s^{-1} .

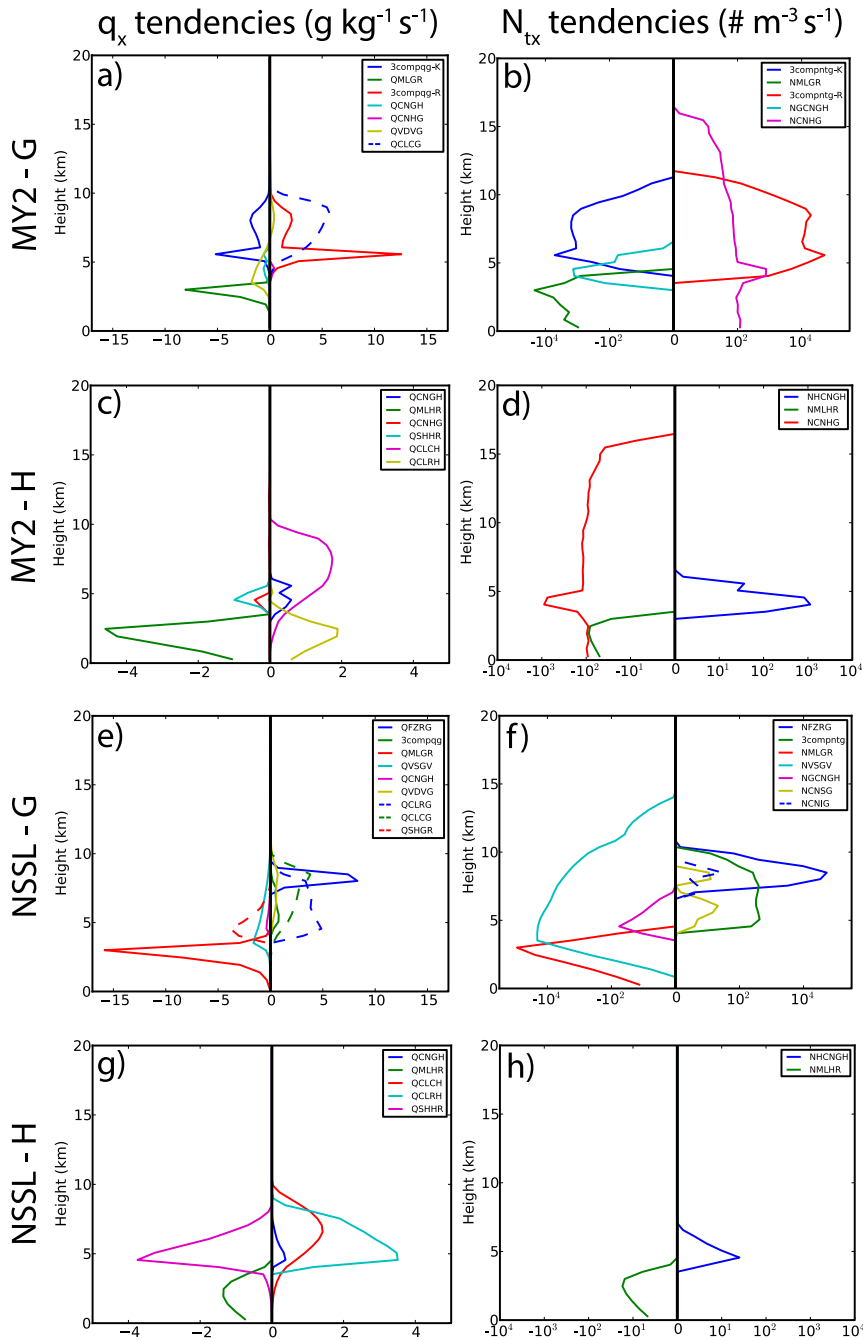


FIG. 11. (left) Vertical mixing ratio q_x ($\text{g kg}^{-1} \text{s}^{-1}$) and (right) number concentration N_{tx} ($\text{m}^{-3} \text{s}^{-1}$) average microphysical tendencies for MY2 (a),(b) graupel and (c),(d) hail, and NSSL (e),(f) graupel and (g),(h) hail. The vertical black line in each plot denotes the zero line separating source and sink terms.

melting level in the MY2 scheme, while graupel number is typically depleted by sublimation of small graupel particles in the NSSL scheme.

Graupel conversion to hail is the primary number source (i.e., creation) of hail in the MY2 and NSSL schemes (Figs. 11d,h). Graupel mass conversion to hail

in the MY2 scheme is larger than the mass conversion in the NSSL scheme (Figs. 11c,g), but is also nearly two orders of magnitude larger in terms of the peak number. Collection of rain and cloud water are the largest sources of hail mass growth in MY2 and NSSL schemes, which again makes sense given the expected wet growth

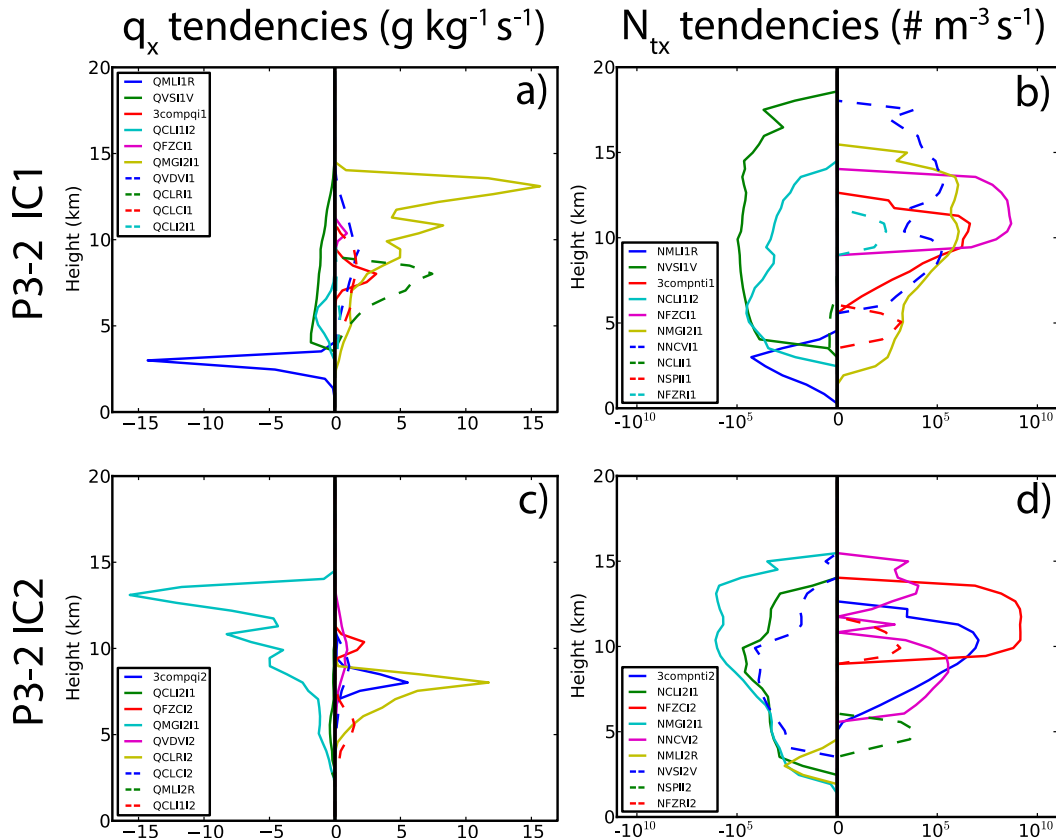


FIG. 12. As in Fig. 11, but for P3–2 (a),(b) iceCat 1 and (c),(d) iceCat 2.

in a supercell updraft. However, the large amount of hail collecting rain below the melting level in the MY2 scheme is rather excessive, and has been documented in Labriola et al. (2017). Melting is the main mass sink below the melting level in the MY2 and NSSL schemes but is much larger in the MY2 scheme. Since large hail reaches the surface in both schemes, MY2 hail collecting rain below the melting level seems to be compensating for the stronger melting.

The merging of iceCat2 to iceCat 1 is the primary source of iceCat 1 mass in the P3–2 scheme (Fig. 12a). We emphasize here that the merging of similar free ice categories in P3 is purely a computational process to free up an additional ice category, and is not a “conversion” process as in traditional BMPs (e.g., conversion of cloud ice to snow). It is reasonable for this merging to increase at higher altitudes, as newly initiated ice or small ice advected through the updraft does not have time to grow to unique sizes. iceCat 1 collecting rain is the second largest source of q_{i1} , echoing the dominant rimed ice growth mechanisms in the MY2 and NSSL schemes. Because free ice categories in P3–2 are not predefined rimed ice categories, processes such as nucleation and freezing cloud water add iceCat 1 number (Fig. 12b).

Dilution of the ice PSD from small ice particle initiation could be problematic in a deep convective framework, as this small nucleated ice could substantially shift the average properties of existing rimed ice. In terms of mass depletion, melting is the dominant process and is abrupt below the melting level. Consequently, whereas melting hail remains at the lowest model level in both the MY2 and NSSL schemes, strong melting leaves little iceCat 1 at this level. Again, this rapid ice depletion is likely a consequence of the P3–2’s restrictive maximum D_{ni} limit prohibiting large particle growth; this is discussed in more detail below. Similar to N_{i1} sources, N_{i1} sinks vary considerably with height: sublimation dominates upper levels, collection is prominent above the melting level, while melting dominates below. IceCat 2 mass in P3–2 is largely affected by two processes: collecting rain for growth, and merging to iceCat 1 as a sink (Fig. 12c). Despite little constraint on the ice type with its free category approach, P3–2 seems to capture well the important rimed ice process of collecting liquid. iceCat 2 is similar to iceCat 1 in that the number sources and sinks vary with height, though merging to iceCat 1 largely dominates depletion of iceCat 2 (Fig. 12d).

TABLE 2. Ice microphysical processes in the superscript: MY2 (M), NSSL (N), and P3–2 (P) schemes. Processes that have been filtered are not included.

Process name	Description
3compqg ^{M,N}	Three-component mass freezing to graupel
QCLCG ^{M,N}	Graupel mass collection of cloud water
QCLCH ^{M,N}	Hail mass collection of cloud water
QCLRG ^N	Graupel mass collection of rain
QCLRH ^{M,N}	Hail mass collection of rain
QCNGH ^{M,N}	Graupel mass conversion to hail
QCNHG ^M	Hail mass conversion to graupel
QFZRG ^N	Freezing rain mass to graupel
QMLGR ^{M,N}	Graupel mass melting to rain
QMLHR ^{M,N}	Hail mass melting to rain
QSHGR ^N	Graupel mass shedding rain
QSHHR ^{M,N}	Hail mass shedding rain
QVDVG ^{M,N}	Graupel mass depositional growth
QVSGV ^N	Graupel mass sublimation
3compqi1 ^P	Three-component mass freezing to iceCat 1
3compqi2 ^P	Three-component mass freezing to iceCat 2
QCLCI1 ^P	IceCat 1 mass collection of cloud water
QCLCI2 ^P	IceCat 2 mass collection of cloud water
QCLI1I2 ^P	IceCat 2 mass collection of iceCat 1
QCLI2I1 ^P	IceCat 1 mass collection of iceCat 2
QCLRI1 ^P	IceCat 1 mass collection of rain
QCLRI2 ^P	IceCat 2 mass collection of rain
QFZCI1 ^P	Freezing cloud water mass to iceCat 1
QFZCI2 ^P	Freezing cloud water mass to iceCat 2
QMG1I1 ^P	IceCat 2 mass merging to iceCat 1
QMLI1R ^P	IceCat 1 mass melting to rain
QMLI2R ^P	IceCat 2 mass melting to rain
QVDVI1 ^P	IceCat 1 mass depositional growth
QVDVI2 ^P	IceCat 2 mass depositional growth
QVSI1V ^P	IceCat 1 mass sublimation
3compntg ^{M,N}	Three-component number freezing to graupel
NGCNGH ^{M,N}	Graupel sink number conversion to hail
NHCNGH ^{M,N}	Graupel number conversion to hail source
NCNHG ^M	Hail number conversion to graupel
NCNIG ^N	Cloud ice number conversion to graupel
NCNSG ^N	Snow number conversion to graupel
NFZRG ^N	Freezing rain number to graupel
NMLGR ^{M,N}	Graupel number melting to rain
NMLHR ^{M,N}	Hail number melting to rain
NVSGV ^N	Graupel number sublimation
3compnti1 ^P	Three-component number freezing to iceCat 1
3compnti2 ^P	Three-component number freezing to iceCat 2
NCLI1I2 ^P	IceCat 2 number collection of iceCat 1
NCLI2I1 ^P	IceCat 1 number collection of iceCat 2
NCLII1 ^P	IceCat 1 number self-collection
NFZCI1 ^P	Freezing cloud water number to iceCat 1
NFZCI2 ^P	Freezing cloud water number to iceCat 2
NFZRI1 ^P	Freezing rain number to iceCat 1
NFZRI2 ^P	Freezing rain number to iceCat 2
NMG1I1 ^P	IceCat 2 number merging to iceCat 1
NMLI1R ^P	IceCat 1 number melting to rain
NMLI2R ^P	IceCat 2 number melting to rain
NNCV1I ^P	IceCat 1 number nucleation
NNCV2I ^P	IceCat 2 number nucleation
NSPII1 ^P	IceCat 1 number splintering
NSPII2 ^P	IceCat 2 number splintering
NVSI1V ^P	IceCat 1 number sublimation
NVSI2V ^P	IceCat 2 number sublimation

b. Size sorting

We create rain and ice mass-weighted mean diameter D_m contoured frequency by altitude diagrams (CFADs; Yuter and Houze 1995) to illustrate the size sorting of rain and ice hydrometeors (Fig. 13). We normalize these frequencies by the number of grid points with a nonzero D_m ; D_{mr} bins are spaced by 0.25 mm, while the analysis for ice uses a 0.5 mm interval. Rain size sorting is clear in the MY2 and NSSL schemes, as D_{mr} frequency increases with decreasing height (Figs. 13a,d). MY2 D_{mr} frequencies favor larger rain diameters at low altitudes due to excessive size sorting (e.g., Wacker and Seifert 2001; Milbrandt and Yau 2005a; Milbrandt and McTaggart-Cowan 2010), while the NSSL scheme modifies N_i to prevent spurious large reflectivity (Mansell 2010). Rain frequencies above the melting level in the schemes are typically near the updraft, revealing that both the MY2 and NSSL schemes carry supercooled water above the melting level. Rimed-ice size sorting potentially drives the Z_{DR} arc signature (Dawson et al. 2014), which is apparent in MY2 and NSSL graupel and hail frequency plots (Figs. 13b,c,e,f). Both rimed-ice categories in both schemes show a clear D_m increase with decreasing height. MY2 rimed ice size sorts at a greater rate, a consequence of the previously mentioned NSSL N_i modification limiting rimed ice size sorting in the scheme. One major difference between this MY2 hail CFAD and the one in Johnson et al. (2016) is the absence of small hail particles. For this study, the default MY2 hail-to-graupel conversion threshold is 1 mm, while the previous threshold in Johnson et al. (2016) was reduced from the default 5 mm to 0 mm. Allowing small hail to be converted to graupel in this study likely led to less small hail particles produced, and allows the scheme to produce more realistic, larger hail.

P3–2 ice overwhelmingly melts to a narrow rain diameter range, typically between 3.0 and 3.25 mm below the melting level (Fig. 13g). The relative maxima at smaller diameters are the result of small raindrops in and near the updrafts due to warm rain processes (e.g., autoconversion). The D_{mr} dominance in one diameter bin is consistent with the P3–2 scheme’s inability to simulate a Z_{DR} arc due to lack of rain size sorting, which is evident from the near constant D_{mr} with decreasing height. On the other hand, D_{mi1} and D_{mi2} both show clear size increase with decreasing height (Figs. 13h,i), suggesting that melting produces uniform raindrop size regardless of ice size. Both P3–2 ice categories show a larger range of mean size than graupel and hail in the other two schemes, a reflection of the numerous modes of ice growth for these “free” categories. While iceCat 1 contoured frequency is more continuous, iceCat 2 displays

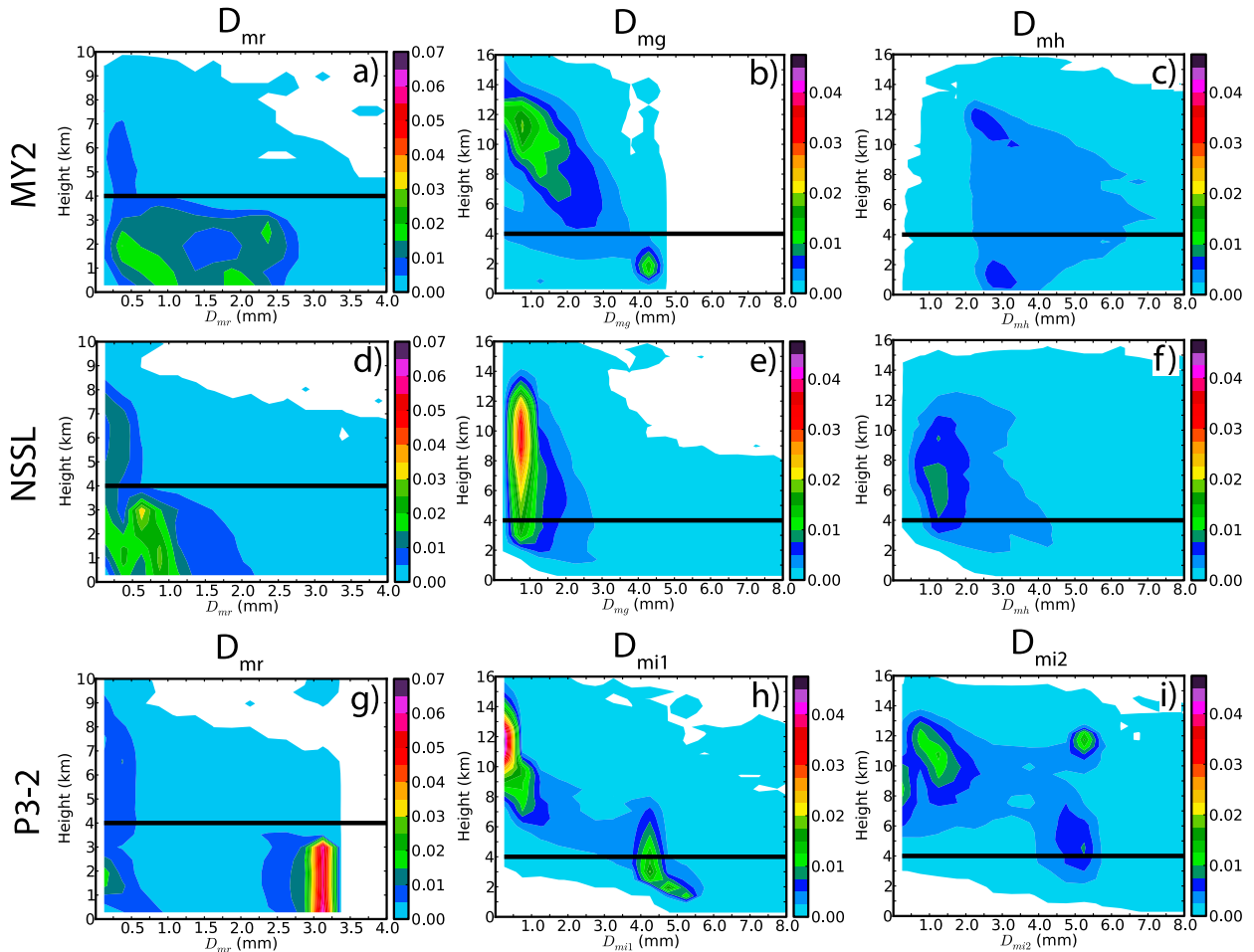


FIG. 13. Contoured frequency by altitude diagrams (CFADs) with rain, graupel, and hail mass-weighted mean diameter D_m (mm) for the (a)–(c) MY2 and (d)–(f) NSSL BMPs, and rain, ice category 1, and ice category 2 for the (g)–(i) P3–2 scheme at $t = 100$ min. The approximate melting level is denoted by a horizontal black line.

more discrete maxima. This is due to the discrete nature of iceCat 2, which can merge with iceCat 1. At $z = 12$ km, iceCat 2 contains a second frequency maximum in the D_{mi2} 5.0–5.5 mm bin, as the particles are prominent in the supercell’s forward flank. Their occurrence decreases directly below this height, before increasing frequency again near $z = 8$ km.

Like other BMPs, P3–2 constricts the rain PSD slope parameter Λ_r to prevent unrealistically small (large Λ_r) or large (small Λ_r) mean drop sizes by explicitly setting Λ_r bounds. Because small drops on the western flank in the P3–2 supercell show evidence of size sorting while larger drops in the forward flank do not (Fig. 2f), the default minimum rain PSD slope bound $\Lambda_{r,\min}$ is likely disrupting the P3–2 surface drop size gradient by preventing the presence of large raindrops on the southern flank of the storm. The sensitivity of mean raindrop size gradient to $\Lambda_{r,\min}$ is explored by reducing $\Lambda_{r,\min}$; it is scaled by a factor of 0.2 (referred to as P3–2_0.2 $\Lambda_{r,\min}$;

Fig. 14). Reducing $\Lambda_{r,\min}$ increases the potential for smaller rain PSD slope near the surface, which shifts the rain distribution to larger drops. Near the surface, D_{mr} in P3–2_0.2 $\Lambda_{r,\min}$ is larger than 5 mm on the supercell’s southern flank, and displays a sharper drop size gradient into the forward flank than in the default P3–2 scheme. The resulting Z_{DR} field exceeds 4 dB near the southern flank, and generally decreases following rain size. While the Z_{DR} gradient in P3–2_0.2 $\Lambda_{r,\min}$ is improved compared to the default P3–2 scheme, enhanced Z_{DR} on the southern flank unrealistically extends too far east of the updraft and does not preferentially decrease in the general direction of the deep-layer storm-relative mean wind vector (as is often observed). However, this is expected behavior given the iceCat 1 distribution above the melting level (Fig. 6e), where ice particles (which are unable to reach the large sizes of MY2 hail and NSSL rimed ice) are also advected well to the east of the updraft, and the sorting of rain particles

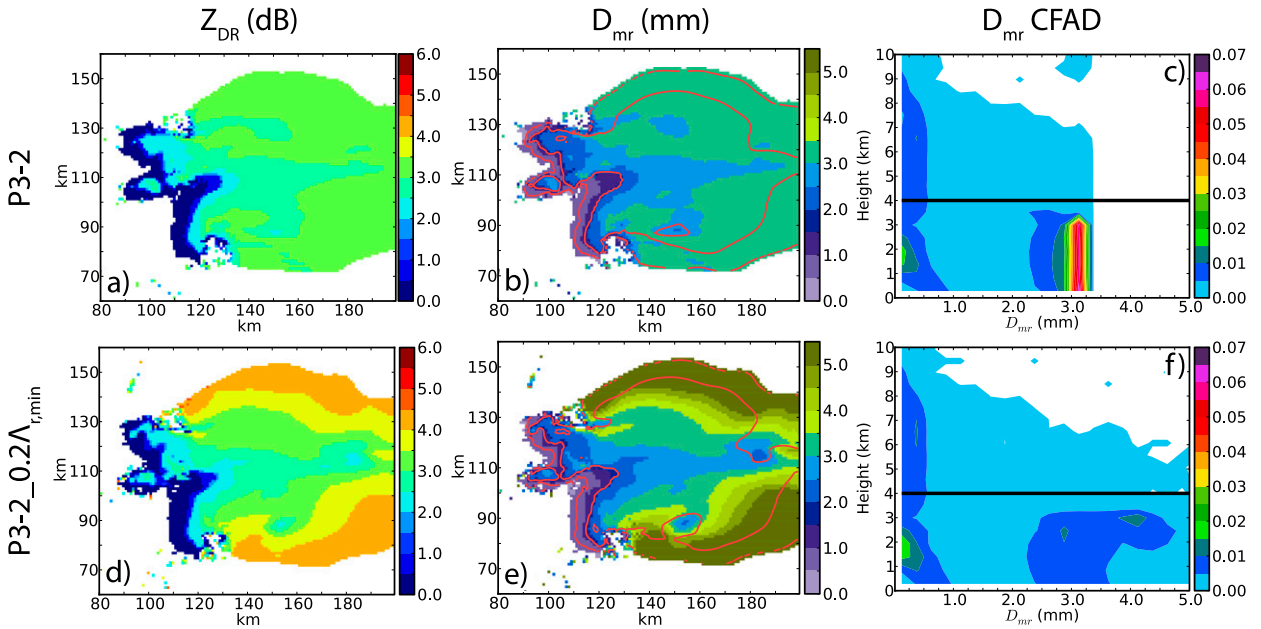


FIG. 14. Differential reflectivity Z_{DR} (dB) and rain mass-weighted mean diameter D_{mr} (mm) near $z \sim 280$ m, and contoured frequency by altitude diagrams (CFADs) with rain mass-weighted mean diameter D_{mr} for the P3-2 (a)–(c) default scheme and (d)–(f) with minimum rain lambda $\Lambda_{r,min}$ reduced by 0.2 at $t = 100$ min. Horizontal reflectivity Z_H contours are overlaid in 20 dBZ intervals starting at 15 dBZ on D_{mr} plots, and the approximate melting level in rain CFAD plots is denoted by a horizontal black line.

by low-level storm-relative winds to the west. Rain CFADs demonstrate that relatively large mean raindrop sizes ($D_{mr} \geq 2$ mm) below the melting level are rather uniform with height in both the default P3-2 and P3-2_0.2 $\Lambda_{r,min}$ (Figs. 14c,f). However, P3-2_0.2 $\Lambda_{r,min}$ simulates a much broader range of mean raindrop sizes and, therefore, more variability of D_{mr} and an improved surface rain size gradient.

c. P3-2 large ice treatment

One key difference between the simulation with the P3-2 scheme and those with MY2 and NSSL is the absence of large ice in the P3-2 run sedimenting to the lowest model level. The default P3 scheme limits the maximum ice number-weighted mean size D_{ni} to 2 mm, which potentially limits the ice growth and accelerates melting. Therefore, we analyze additional sensitivity tests with maximum D_{ni} limit set to 7 mm (D_{ni_7}) and 12 mm (D_{ni_12}) to examine the relationship between this limit and ice sedimenting to the surface (Fig. 15). Indeed, the gradual relaxation of this limit continually increases both the size and frequency of ice reaching the surface. Therefore, the default P3-2 is not removing rimed ice at a greater rate than other BMPs by design, but rather not producing large enough ice at the surface due to the restrictive D_{ni} limit. Mass-weighted mean diameter of iceCat 1 D_{mi1} and iceCat 2 D_{mi2} in both D_{ni} tests regularly exceed 12 mm, which is

closer to the surface hail size in MY2 and NSSL than the default P3-2 D_{mi1} and D_{mi2} . As a result, this larger ice reduces Z_{DR} near the observed hail signature location (Kumjian and Ryzhkov 2008), but also unphysically sediments into the forward flank as the mass-weighted fall speed of both P3-2 ice categories are typically smaller than MY2 and NSSL hail.

To quantify the relationship between P3-2 large ice production and its maximum D_{ni} limit, Fig. 16 shows a time series of domain-averaged maximum rimed-ice size (“mean max diameter”) in the updraft (vertical velocity $w > 10 \text{ m s}^{-1}$) for the default BMPs and D_{ni} limit sensitivity tests. We define maximum rimed-ice size as the largest diameter for which the PSD number density $N(D)$ exceeds $10^{-4} \text{ m}^{-3} \text{ mm}^{-1}$ (Snook et al. 2016; Labriola et al. 2017). We additionally impose a constraint of rime fraction $f_r > 0.9$ in P3-2 to ensure the ice is sufficiently rimed to be labeled as “rimed ice” following the traditional BMP nomenclature, allowing for greater consistency with MY2 and NSSL large ice production. A natural separation exists between graupel and hail in the MY2 and NSSL schemes, with maximum hail size ranging between 18 and 27 mm and graupel between 8 and 14 mm after 40 min (Fig. 16a). Indeed, the default P3-2 categories also follow this separation with iceCat 1 tending to resemble the hail categories in MY2 and NSSL while iceCat 2 tends to resemble graupel in these simulations. As iceCat 2 always merges to iceCat 1, it

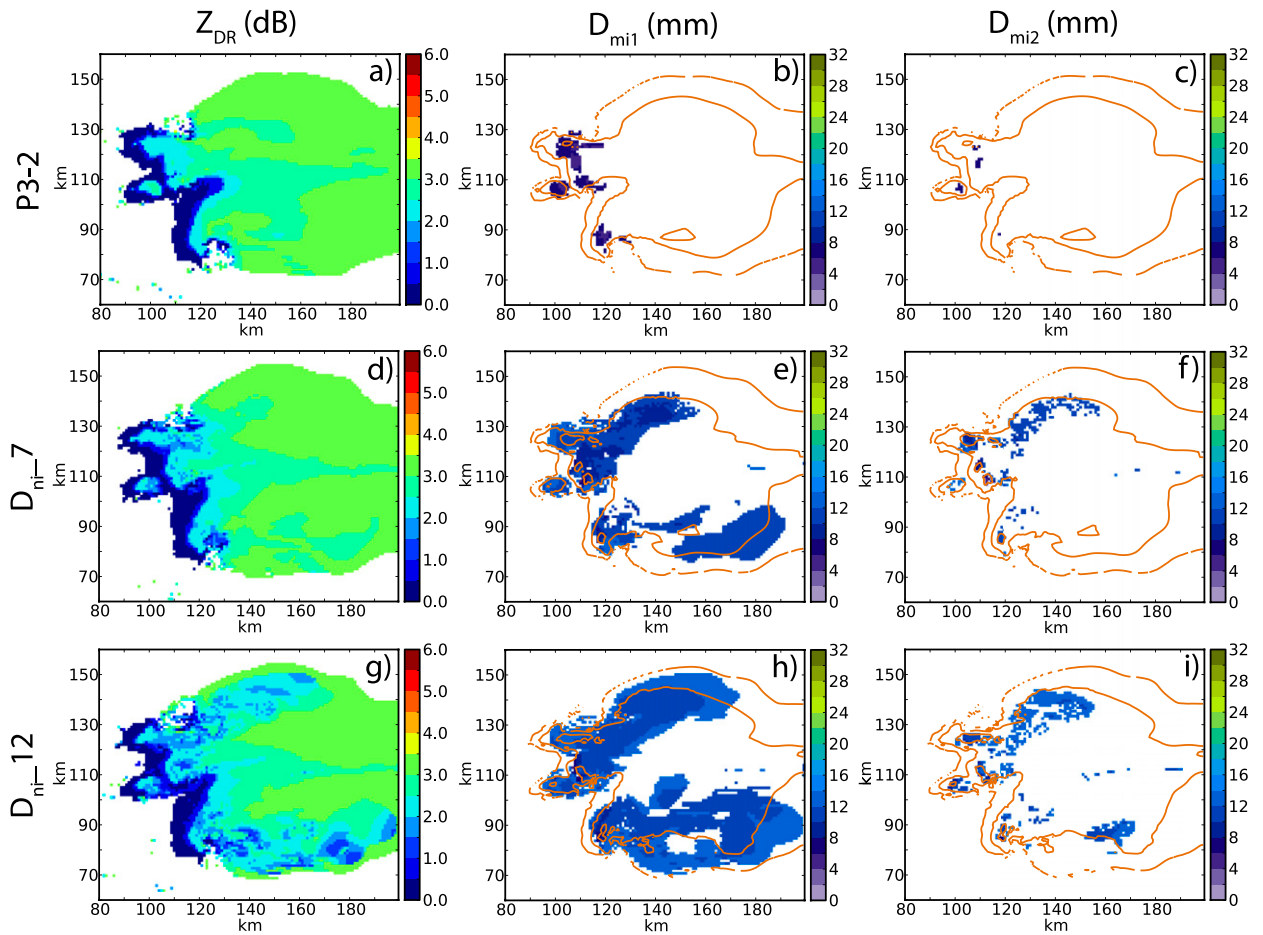


FIG. 15. Differential reflectivity Z_{DR} (dB), and mass-weighted mean diameter of iceCat 1 D_{mi1} (mm) and iceCat 2 D_{mi2} (mm) near $z = \sim 280$ m for the P3-2 (a)–(c) default scheme, (d)–(f) with the maximum ice number-weighted mean diameter limit set to 7 mm, and (g)–(i) 12 mm at $t = 100$ min. Horizontal reflectivity Z_H contours are overlaid in 20 dBZ intervals starting at 15 dBZ on D_{mi} plots.

appears iceCat 2 does not have sufficient time to reach iceCat 1 sizes in the updraft. Maximum iceCat 1 size in the default P3-2 scheme is generally smaller than hail in the other bulk schemes, limiting the sedimentation of

ice to the surface. When relaxing the maximum D_{ni} limit, both iceCat 1 and 2 increase in size, with D_{ni_7} and D_{ni_12} iceCat 2 exceeding MY2 and NSSL maximum graupel size, and D_{ni_7} and D_{ni_12} iceCat 1 following

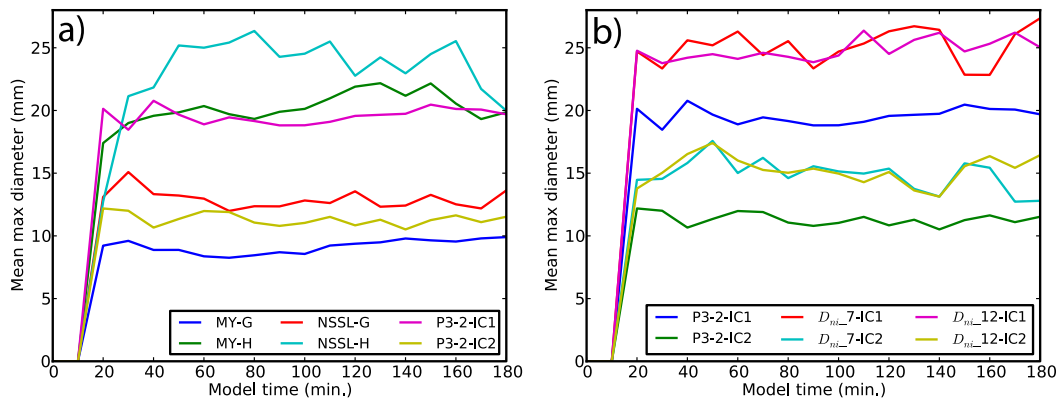


FIG. 16. Mean max diameter (mm) of rimed ice in the updraft for the (a) MY2, NSSL, and P3-2 BMPs and (b) P3-2 maximum ice number-weighted mean diameter limit tests over the duration of the model run.

NSSL hail more closely after $t = 40$ min (Fig. 16b). Therefore, relaxing the maximum D_{ni} limit clearly increases the occurrence of large rimed ice in P3–2, which in turn is able to sediment to the surface. This relationship is not simply one-to-one, as the D_{ni-7} iceCat 1 and 2 sizes exceed D_{ni-12} iceCat 1 and 2 at times during the simulations despite having a more stringent maximum D_{ni} limit. This indicates that while relaxing the D_{ni} limit clearly increases the potential for rimed ice to grow large in the scheme, the degree to which ice grows depends more on the ice growth processes themselves rather than the D_{ni} limit.

5. Summary and discussion

We perform idealized supercell simulations using WRF v3.9.1 to determine how the representation of rimed ice in bulk microphysics schemes can explain the presence or lack of polarimetric signatures. The BMPs examined are the two-moment versions of Milbrandt–Yau (MY2), National Severe Storms Laboratory (NSSL), and the two-category configuration of the P3 scheme (P3–2). The simulated polarimetric signatures considered are the Z_{DR} arc and the hail signature in the forward-flank downdraft, which are particularly sensitive to rimed-ice representation. Both the MY2 and NSSL BMPs are generally able to simulate a Z_{DR} decrease in the direction of the deep-layer storm-relative mean wind vector near the surface (though weakly in MY2), but are unable to simulate a Z_{DR} arc entirely consistent with observations. The P3–2 scheme simulates a weak Z_{DR} gradient in the forward flank, despite containing two-moment rain and two two-moment free ice categories. Reducing the scheme’s restrictive minimum rain PSD slope $\Lambda_{r,min}$ limit facilitates a Z_{DR} gradient more consistent with observations than in the default P3–2 scheme, but also simulates a Z_{DR} arc extending well into the forward flank and an associated Z_{DR} gradient that fails to preferentially decrease in the general direction of the deep-layer storm-relative mean wind vector as is often observed (although this gradient is consistent with rain sorting by low-level storm-relative winds in the simulated storm). Therefore, other aspects of P3–2 that affect size sorting may require future improvement to better simulate the Z_{DR} arc.

Only the NSSL scheme simulates the location of the hail signature in the FFD most consistent with observations. The MY2 scheme does produce large hail that easily reaches the surface but it generally appears on the southern flank of the supercell. Larger hail with nonzero water fraction in the MY2 scheme contains more particles prone to the resonance effect than the NSSL scheme, and therefore simulates a larger ρ_{HV} reduction in the

hail signature location. Ice in the default P3–2 is generally unable to reach the surface, and the small, wet particles that do reach the surface increase Z_{DR} . Surface ρ_{HV} in the scheme is consequently large, and typically reduced by large, oblate drops rather than resonance-sized ice particles. The default P3–2 restricts the maximum ice number-weighted mean size D_{ni} to 2 mm, and produces larger ice that reaches the surface and reduces Z_{DR} when this limiter is relaxed. However, these particles also unphysically sediment into the forward flank due to the relatively small ice mass-weighted fall speeds compared to MY2 and NSSL hail, implying that further investigation of the maximum D_{ni} limit is needed.

Whereas MY2 graupel generally forms by 3-component freezing, NSSL graupel is typically formed from freezing rain in these idealized supercell simulations. The primary hail origin in the MY2 and NSSL schemes is graupel. Although MY2 and NSSL hail origin are similar, MY2 hail has a smaller horizontally averaged mass-weighted mean fall speed than NSSL hail over the depth of the model domain while MY2 graupel does not reach the large graupel sizes in the NSSL scheme and has a typically smaller fall speed curve than NSSL graupel, enhancing the downstream advection of rimed ice in the scheme. Therefore, increasing MY2 rimed ice fall speed and simulating larger graupel particles could improve the scheme’s simulated polarimetric signatures by suppressing rimed ice horizontal advection (although the supercell in this simulation enhances rimed ice downstream advection with a stronger northwesterly storm-relative mean wind near the updraft, likely linked to the BMP’s microphysical feedback with ambient thermodynamics as each simulation is initialized with the same shear profile). Integral to the growth of ice in each scheme is the collection of liquid, though MY2 hail seems to excessively collect rain below the melting level. P3–2 iceCat 1 melting is more comparable to MY2 and NSSL graupel melting, a reflection of its restrictive maximum D_{ni} limiter (default value of 2 mm) producing relatively small ice particle mean sizes.

At this point, it is worth reiterating the P3’s treatment of ice, particularly rimed ice. In the scheme, a single PSD contains all ice modes, including small spherical, larger nonspherical, and rimed ice. The degree to which rimed ice occupies the ice PSD depends on the rime fraction, which for the idealized supercell case examined in this paper is frequently large due to the storm’s dominant mode of riming growth. This BMP framework can be problematic in some situations when newly initiated small ice is assigned to an ice category dominated by rimed ice. Such a process would “dilute” the category by increasing the amount of small ice within the category’s PSD, and the category’s processes (e.g., riming growth, melting) would subsequently become more reflective

of small ice (Milbrandt and Morrison 2016). While “dilution” is a common problem for any bulk microphysics scheme when very different PSDs that have experienced different evolutions are mixed together at a given point (e.g., large hail sedimenting into a grid box where small hail is being initiated), the P3 BMP might be more susceptible to this problem because all ice modes exist in one PSD for each category. Still, this P3 rimed ice dilution could be mitigated by increasing the number of ice categories or modifying new ice category destination based on its initiation process (i.e., having separate categories initiated by ice nucleation/freezing of small drops and freezing of large drops).

The P3–2’s default maximum ice number-weighted mean diameter limit of 2 mm is overly restrictive for modeling hail. A fairly restrictive limiter when riming is unimportant may be necessary as there is no explicit representation of snow particle breakup in P3 (although most BMPs neglect explicit snow breakup). Hence, relaxing the limit improved the performance of the scheme in terms of its simulation of large rimed ice near the surface, but has the potential to grow unrimed or lightly rimed nonspherical ice in the scheme too large. Future work should investigate this problem further. It may be possible to apply a more sophisticated size limiter that varies with ice properties such as rime fraction. Another possibility could be to add an explicit parameterization of snow particle breakup and relax the size limiter. A three-moment ice version of P3 evolving the size distribution shape parameter explicitly is currently in development, which may also obviate the need for a restrictive size limiter. Also, a prognostic liquid fraction on ice has recently been developed for P3 (Cholette et al. 2019); future work will examine the effects of this on the simulation of melting hail and the impacts on simulated polarimetric signatures. Overall, the results of this study suggest it is important to compare newly designed microphysics schemes with existing, state-of-the-art schemes to understand their behaviors and performance, and to identify the shortcomings of these schemes so that they can be further improved.

Acknowledgments. This research was primarily supported by the NOAA Warn-on-Forecast (WoF) Grant NA16OAR4320115. We also thank three anonymous reviewers who greatly improved the quality of this manuscript.

REFERENCES

- Brandes, E. A., G. Zhang, and J. Vivekanandan, 2002: Experiments in rainfall estimation with a polarimetric radar in a subtropical environment. *J. Appl. Meteor.*, **41**, 674–685, [https://doi.org/10.1175/1520-0450\(2002\)041<0674:EIREWA>2.0.CO;2](https://doi.org/10.1175/1520-0450(2002)041<0674:EIREWA>2.0.CO;2).
- Cao, Q., G. Zhang, E. Brandes, T. Schuur, A. Ryzhkov, and K. Ikeda, 2008: Analysis of video disdrometer and polarimetric radar data to characterize rain microphysics in Oklahoma. *J. Appl. Meteor. Climatol.*, **47**, 2238–2255, <https://doi.org/10.1175/2008JAMC1732.1>.
- Chandrasekar, V., W. A. Cooper, and V. N. Bringi, 1988: Axis ratios and oscillations of raindrops. *J. Atmos. Sci.*, **45**, 1323–1333, [https://doi.org/10.1175/1520-0469\(1988\)045<1323:ARAOOR>2.0.CO;2](https://doi.org/10.1175/1520-0469(1988)045<1323:ARAOOR>2.0.CO;2).
- Cholette, M., H. Morrison, J. A. Milbrandt, and J. M. Thériault, 2019: Parameterization of the bulk liquid fraction on mixed-phase particles in the predicted particle properties (P3) scheme: Description and idealized simulations. *J. Atmos. Sci.*, **76**, 561–582, <https://doi.org/10.1175/JAS-D-18-0278.1>.
- Dawson, D. T., M. Xue, J. A. Milbrandt, and M. K. Yau, 2010: Comparison of evaporation and cold pool development between single-moment and multimoment bulk microphysics schemes in idealized simulations of tornadic thunderstorms. *Mon. Wea. Rev.*, **138**, 1152–1171, <https://doi.org/10.1175/2009MWR2956.1>.
- , E. R. Mansell, Y. Jung, L. J. Wicker, M. R. Kumjian, and M. Xue, 2014: Low-level Z_{DR} signatures in supercell forward flanks: The role of size sorting and melting of hail. *J. Atmos. Sci.*, **71**, 276–299, <https://doi.org/10.1175/JAS-D-13-0118.1>.
- , —, and M. R. Kumjian, 2015: Does wind shear cause hydrometeor size sorting? *J. Atmos. Sci.*, **72**, 340–348, <https://doi.org/10.1175/JAS-D-14-0084.1>.
- Fan, J., and Coauthors, 2017: Cloud-resolving model intercomparison of an MC3E squall line case: Part I—Convective updrafts. *J. Geophys. Res. Atmos.*, **122**, 9351–9378, <https://doi.org/10.1002/2017JD026622>.
- Ferrier, B. S., 1994: A double-moment multiple-phase four-class bulk ice scheme. Part I: Description. *J. Atmos. Sci.*, **51**, 249–280, [https://doi.org/10.1175/1520-0469\(1994\)051<0249:ADMMPF>2.0.CO;2](https://doi.org/10.1175/1520-0469(1994)051<0249:ADMMPF>2.0.CO;2).
- Johnson, D. E., P. K. Wang, and J. M. Straka, 1993: Numerical simulation of the 2 August 1981 CCOPE supercell storm with and without ice microphysics. *J. Appl. Meteor.*, **32**, 745–759, [https://doi.org/10.1175/1520-0450\(1993\)032<0745:NSOTAC>2.0.CO;2](https://doi.org/10.1175/1520-0450(1993)032<0745:NSOTAC>2.0.CO;2).
- Johnson, M., Y. Jung, D. T. Dawson II, and M. Xue, 2016: Comparison of simulated polarimetric signatures in idealized supercell storms using two-moment bulk microphysics schemes in WRF. *Mon. Wea. Rev.*, **144**, 971–996, <https://doi.org/10.1175/MWR-D-15-0233.1>.
- , —, D. Dawson, T. Supinie, M. Xue, J. Park, and Y.-H. Lee, 2018: Evaluation of unified model microphysics in high-resolution NWP simulations using polarimetric radar observations. *Adv. Atmos. Sci.*, **35**, 771–784, <https://doi.org/10.1007/s00376-017-7177-0>.
- Jung, Y., G. Zhang, and M. Xue, 2008: Assimilation of simulated polarimetric radar data for a convective storm using the ensemble Kalman filter. Part I: Observation operators for reflectivity and polarimetric variables. *Mon. Wea. Rev.*, **136**, 2228–2245, <https://doi.org/10.1175/2007MWR2083.1>.
- , M. Xue, and G. Zhang, 2010: Simulations of polarimetric radar signatures of a supercell storm using a two-moment bulk microphysics scheme. *J. Appl. Meteor. Climatol.*, **49**, 146–163, <https://doi.org/10.1175/2009JAMC2178.1>.
- , —, and M. Tong, 2012: Ensemble Kalman filter analyses of the 29–30 May 2004 Oklahoma tornadic thunderstorm using one- and two-moment bulk microphysics schemes, with verification against polarimetric radar data.

- Mon. Wea. Rev.*, **140**, 1457–1475, <https://doi.org/10.1175/MWR-D-11-00032.1>.
- Khain, A., A. Pokrovsky, M. Pinsky, A. Seifert, and V. Phillips, 2004: Simulation of effects of atmospheric aerosols on deep turbulent convective clouds using a spectral microphysics mixed-phase cumulus cloud model. Part I: Model description and possible applications. *J. Atmos. Sci.*, **61**, 2963–2982, <https://doi.org/10.1175/JAS-3350.1>.
- Klemp, J. B., 1987: Dynamics of tornadic thunderstorms. *Annu. Rev. Fluid Mech.*, **19**, 369–402, <https://doi.org/10.1146/annurev.fl.19.010187.002101>.
- , and R. B. Wilhelmson, 1978: Simulations of right- and left-moving storms produced through storm splitting. *J. Atmos. Sci.*, **35**, 1097–1110, [https://doi.org/10.1175/1520-0469\(1978\)035<1097:SORALM>2.0.CO;2](https://doi.org/10.1175/1520-0469(1978)035<1097:SORALM>2.0.CO;2).
- Kumjian, M. R., and A. V. Ryzhkov, 2008: Polarimetric signatures in supercell thunderstorms. *J. Appl. Meteor. Climatol.*, **47**, 1940–1961, <https://doi.org/10.1175/2007JAMC1874.1>.
- , and —, 2009: Storm-relative helicity revealed from polarimetric radar measurements. *J. Atmos. Sci.*, **66**, 667–685, <https://doi.org/10.1175/2008JAS2815.1>.
- , and —, 2012: The impact of size sorting on the polarimetric radar variables. *J. Atmos. Sci.*, **69**, 2042–2060, <https://doi.org/10.1175/JAS-D-11-0125.1>.
- Labriola, J., N. Snook, Y. Jung, B. Putnam, and M. Xue, 2017: Ensemble hail prediction for the storms of 10 May 2010 in south-central Oklahoma using single- and double-moment microphysical schemes. *Mon. Wea. Rev.*, **145**, 4911–4936, <https://doi.org/10.1175/MWR-D-17-0039.1>.
- Liu, X., J. E. Penner, S. J. Ghan, and M. Wang, 2007: Inclusion of ice microphysics in the NCAR community atmospheric model version 3 (CAM3). *J. Climate*, **20**, 4526–4547, <https://doi.org/10.1175/JCLI4264.1>.
- Loftus, A. M., W. R. Cotton, and G. G. Carrió, 2014: A triple-moment hail bulk microphysics scheme. Part I: Description and initial evaluation. *Atmos. Res.*, **149**, 35–57, <https://doi.org/10.1016/j.atmosres.2014.05.013>.
- Mansell, E. R., 2010: On sedimentation and advection in multimoment bulk microphysics. *J. Atmos. Sci.*, **67**, 3084–3094, <https://doi.org/10.1175/2010JAS3341.1>.
- , C. L. Ziegler, and E. C. Bruning, 2010: Simulated electrification of a small thunderstorm with two-moment bulk microphysics. *J. Atmos. Sci.*, **67**, 171–194, <https://doi.org/10.1175/2009JAS2965.1>.
- Milbrandt, J. A., and M. K. Yau, 2005a: A multimoment bulk microphysics parameterization. Part I: Analysis of the role of the spectral shape parameter. *J. Atmos. Sci.*, **62**, 3051–3064, <https://doi.org/10.1175/JAS3534.1>.
- , and —, 2005b: A multimoment bulk microphysics parameterization. Part II: A proposed three-moment closure and scheme description. *J. Atmos. Sci.*, **62**, 3065–3081, <https://doi.org/10.1175/JAS3535.1>.
- , and R. McTaggart-Cowan, 2010: Sedimentation-induced errors in bulk microphysics schemes. *J. Atmos. Sci.*, **67**, 3931–3948, <https://doi.org/10.1175/2010JAS3541.1>.
- , and H. Morrison, 2013: Prediction of graupel density in a bulk microphysics scheme. *J. Atmos. Sci.*, **70**, 410–429, <https://doi.org/10.1175/JAS-D-12-0204.1>.
- , and —, 2016: Parameterization of cloud microphysics based on the prediction of bulk ice particle properties. Part III: Introduction of multiple free categories. *J. Atmos. Sci.*, **73**, 975–995, <https://doi.org/10.1175/JAS-D-15-0204.1>.
- Morrison, H., and J. A. Milbrandt, 2011: Comparison of two-moment bulk microphysics schemes in idealized supercell thunderstorm simulations. *Mon. Wea. Rev.*, **139**, 1103–1130, <https://doi.org/10.1175/2010MWR3433.1>.
- , and —, 2015: Parameterization of cloud microphysics based on the prediction of bulk ice particle properties. Part I: Scheme description and idealized tests. *J. Atmos. Sci.*, **72**, 287–311, <https://doi.org/10.1175/JAS-D-14-0065.1>.
- , G. Thompson, and V. Tatarskii, 2009: Impact of cloud microphysics on the development of trailing stratiform precipitation in a simulated squall line: Comparison of one- and two-moment schemes. *Mon. Wea. Rev.*, **137**, 991–1007, <https://doi.org/10.1175/2008MWR2556.1>.
- , J. A. Milbrandt, G. H. Bryan, K. Ikeda, S. A. Tessendorf, and G. Thompson, 2015: Parameterization of cloud microphysics based on the prediction of bulk ice particle properties. Part II: Case study comparisons with observations and other schemes. *J. Atmos. Sci.*, **72**, 312–339, <https://doi.org/10.1175/JAS-D-14-0066.1>.
- Murakami, M., 1990: Numerical modeling of dynamical and microphysical evolution of an isolated convective cloud—the 19 July 1981 CCOPE cloud. *J. Meteor. Soc. Japan*, **68**, 107–128, https://doi.org/10.2151/jmsj1965.68.2_107.
- Palmer, R. D., and Coauthors, 2011: Observations of the 10 May 2010 tornado outbreak using OU-PRIME: Potential for science with high-resolution polarimetric radar. *Bull. Amer. Meteor. Soc.*, **92**, 871–891, <https://doi.org/10.1175/2011BAMS3125.1>.
- Pruppacher, H. R., and R. L. Pitter, 1971: A semi-empirical determination of the shape of cloud and rain drops. *J. Atmos. Sci.*, **28**, 86–94, [https://doi.org/10.1175/1520-0469\(1971\)028<0086:ASEDOT>2.0.CO;2](https://doi.org/10.1175/1520-0469(1971)028<0086:ASEDOT>2.0.CO;2).
- Putnam, B. J., M. Xue, Y. Jung, N. A. Snook, and G. Zhang, 2014: The analysis and prediction of microphysical states and polarimetric radar variables in a mesoscale convective system using double-moment microphysics, multinet radar data, and the ensemble Kalman filter. *Mon. Wea. Rev.*, **142**, 141–162, <https://doi.org/10.1175/MWR-D-13-00042.1>.
- , —, —, —, and —, 2017a: Ensemble probabilistic prediction of a mesoscale convective system and associated polarimetric radar variables using single-moment and double-moment microphysics schemes and EnKF radar data assimilation. *Mon. Wea. Rev.*, **145**, 2257–2279, <https://doi.org/10.1175/MWR-D-16-0162.1>.
- , —, —, G. Zhang, and F. Kong, 2017b: Simulation of polarimetric radar variables from 2013 CAPS spring experiment storm-scale ensemble forecasts and evaluation of microphysics schemes. *Mon. Wea. Rev.*, **145**, 49–73, <https://doi.org/10.1175/MWR-D-15-0415.1>.
- Rasmussen, R. M., and A. J. Heymsfield, 1987: Melting and shedding of graupel and hail. Part I: Model physics. *J. Atmos. Sci.*, **44**, 2754–2763, [https://doi.org/10.1175/1520-0469\(1987\)044<2754:MASOGA>2.0.CO;2](https://doi.org/10.1175/1520-0469(1987)044<2754:MASOGA>2.0.CO;2).
- Rotunno, R., and J. B. Klemp, 1982: The influence of the shear-induced pressure gradient on thunderstorm motion. *Mon. Wea. Rev.*, **110**, 136–151, [https://doi.org/10.1175/1520-0493\(1982\)110<0136:TIOTSI>2.0.CO;2](https://doi.org/10.1175/1520-0493(1982)110<0136:TIOTSI>2.0.CO;2).
- Rutledge, S. A., and P. V. Hobbs, 1984: The mesoscale and microscale structure and organization of clouds and precipitation in midlatitude cyclones. XII: A diagnostic modeling study of precipitation development in narrow cold-frontal rainbands. *J. Atmos. Sci.*, **41**, 2949–2972, [https://doi.org/10.1175/1520-0469\(1984\)041<2949:TMAMSA>2.0.CO;2](https://doi.org/10.1175/1520-0469(1984)041<2949:TMAMSA>2.0.CO;2).
- Ryzhkov, A. V., T. J. Schuur, D. W. Burgess, and D. S. Zrnic, 2005: Polarimetric tornado detection. *J. Appl. Meteor.*, **44**, 557–570, <https://doi.org/10.1175/JAM2235.1>.

- Skamarock, W. C., and Coauthors, 2008: A description of the Advanced Research WRF version 3. NCAR Tech. Note NCAR/TN-475+STR, 113 pp., <https://doi.org/10.5065/D68S4MVH>
- Snook, N., Y. Jung, J. Brotzge, B. Putnam, and M. Xue, 2016: Prediction and ensemble forecast verification of hail in the supercell storms of 20 May 2013. *Wea. Forecasting*, **31**, 811–825, <https://doi.org/10.1175/WAF-D-15-0152.1>.
- Takahashi, T., 1976: Hail in an axisymmetric cloud model. *J. Atmos. Sci.*, **33**, 1579–1601, [https://doi.org/10.1175/1520-0469\(1976\)033<1579:HIAACM>2.0.CO;2](https://doi.org/10.1175/1520-0469(1976)033<1579:HIAACM>2.0.CO;2).
- Tao, W.-K., and J. Simpson, 1993: Goddard cumulus ensemble model. Part I: Model description. *Terr. Atmos. Oceanic Sci.*, **4**, 35–72, [https://doi.org/10.3319/TAO.1993.4.1.35\(A\)](https://doi.org/10.3319/TAO.1993.4.1.35(A)).
- Thompson, G., P. R. Field, R. M. Rasmussen, and W. D. Hall, 2008: Explicit forecasts of winter precipitation using an improved bulk microphysics scheme. Part II: Implementation of a new snow parameterization. *Mon. Wea. Rev.*, **136**, 5095–5115, <https://doi.org/10.1175/2008MWR2387.1>.
- Van Den Broeke, M. S., 2016: Polarimetric variability of classic supercell storms as a function of environment. *J. Appl. Meteor. Climatol.*, **55**, 1907–1925, <https://doi.org/10.1175/JAMC-D-15-0346.1>.
- Van Weverberg, K., E. Goudenhoofd, U. Blahak, E. Brisson, M. Demuzere, P. Marbaix, and J.-P. van Ypersele, 2014: Comparison of one-moment and two-moment bulk microphysics for high-resolution climate simulations of intense precipitation. *Atmos. Res.*, **147–148**, 145–161, <https://doi.org/10.1016/j.atmosres.2014.05.012>.
- Varble, A., and Coauthors, 2011: Evaluation of cloud-resolving model intercomparison simulations using TWP-ICE observations: Precipitation and cloud structure. *J. Geophys. Res.*, **116**, D12206, <https://doi.org/10.1029/2010JD015180>.
- Vivekanandan, J., W. M. Adams, and V. N. Bringi, 1991: Rigorous approach to polarimetric radar modeling of hydrometeor orientation distributions. *J. Appl. Meteor.*, **30**, 1053–1063, [https://doi.org/10.1175/1520-0450\(1991\)030<1053:RATPRM>2.0.CO;2](https://doi.org/10.1175/1520-0450(1991)030<1053:RATPRM>2.0.CO;2).
- Wacker, U., and A. Seifert, 2001: Evolution of rain water profiles resulting from pure sedimentation: Spectral vs. parameterized description. *Atmos. Res.*, **58**, 19–39, [https://doi.org/10.1016/S0169-8095\(01\)00081-3](https://doi.org/10.1016/S0169-8095(01)00081-3).
- Walko, R. L., W. R. Cotton, M. P. Meyers, and J. Y. Harrington, 1995: New RAMS cloud microphysics parameterization. Part I: The single-moment scheme. *Atmos. Res.*, **38**, 29–62, [https://doi.org/10.1016/0169-8095\(94\)00087-T](https://doi.org/10.1016/0169-8095(94)00087-T).
- Wang, Y., C. N. Long, L. R. Leung, J. Dudhia, S. A. McFarlane, J. H. Mather, S. J. Ghan, and X. Liu, 2009: Evaluating regional cloud-permitting simulations of the WRF model for the Tropical Warm Pool International Cloud Experiment (TWP-ICE), Darwin, 2006. *J. Geophys. Res.*, **114**, D21203, <https://doi.org/10.1029/2009JD012729>.
- Waterman, P. C., 1969: Scattering by dielectric obstacles. *Alta Freq.*, **38**, 348–352.
- Weisman, M. L., and J. B. Klemp, 1982: The dependence of numerically simulated convective storms on vertical wind shear and buoyancy. *Mon. Wea. Rev.*, **110**, 504–520, [https://doi.org/10.1175/1520-0493\(1982\)110<0504:TDonSC>2.0.CO;2](https://doi.org/10.1175/1520-0493(1982)110<0504:TDonSC>2.0.CO;2).
- Wisner, C., H. D. Orville, and C. Myers, 1972: A numerical model of a hail-bearing cloud. *J. Atmos. Sci.*, **29**, 1160–1181, [https://doi.org/10.1175/1520-0469\(1972\)029<1160:ANMOAH>2.0.CO;2](https://doi.org/10.1175/1520-0469(1972)029<1160:ANMOAH>2.0.CO;2).
- Yuter, S. E., and R. A. Houze Jr., 1995: Three-dimensional kinematic and microphysical evolution of Florida cumulonimbus. Part II: Frequency distributions of vertical velocity, reflectivity, and differential reflectivity. *Mon. Wea. Rev.*, **123**, 1941–1963, [https://doi.org/10.1175/1520-0493\(1995\)123<1941:TDKAME>2.0.CO;2](https://doi.org/10.1175/1520-0493(1995)123<1941:TDKAME>2.0.CO;2).
- Zhang, G., J. Vivekanandan, and E. Brandes, 2001: A method for estimating rain rate and drop size distribution from polarimetric radar measurements. *IEEE Trans. Geosci. Remote Sens.*, **39**, 830–841, <https://doi.org/10.1109/36.917906>.
- Ziegler, C. L., 1985: Retrieval of thermal and microphysical variables in observed convective storms. Part I: Model development and preliminary testing. *J. Atmos. Sci.*, **42**, 1487–1509, [https://doi.org/10.1175/1520-0469\(1985\)042<1487:ROTAMV>2.0.CO;2](https://doi.org/10.1175/1520-0469(1985)042<1487:ROTAMV>2.0.CO;2).